Analysis of the HII-Region DEM L 36 in the Large Magellanic Cloud

Master's Thesis in Physics

Presented by
Florian Steynberg

05.03.2024

Dr. Karl Remeis-Sternwarte
Friedrich-Alexander-Universität Erlangen-Nürnberg

Supervisor: Prof. Dr. Manami Sasaki

Zusammenfassung

Das interstellare Medium (ISM) ist ein hochkomplexes Thema, das generell mit Hilfe von numerischen Simulationen erforscht wird. Das ISM kann im Allgemeinen in drei thermale Phasen eingeteilt werden, eine kalte Phase ($10 - 10^2$ K), eine warme Phase ($10^2 - 10^4$ K) und eine heiße Phase ($\gtrsim 10^6\ K$), die auf turbulente Weise miteinander interagieren und dabei Strukturen wie Spiralarme und Superbubbles formen. Hauptsächlich angetrieben von stellaren Winden und Supernovae, nimmt die heiße Phase einen signifikanten Anteil des galaktischen Volumens ein, während sie andererseits weniger als 1% der Masse des interstellaren Mediums ausmacht. In dieser Arbeit wird eine blasenartige Struktur, bei den Koordinaten RA: $04^{\mathrm{h}}57^{\mathrm{m}}07.8^{\mathrm{s}}$ und DEK: $-69^{\circ}23'58.0''$ in der Großen Magellanischen Wolke, im Röntgenspektrum untersucht. Hierzu werden Daten verwendet, die mit dem XMM-Newton Röntgenobservatorium produziert wurden. Obwohl die Daten stark mit Flares kontaminiert sind, zeigen die Bilder deutlich eine Region mit diffuser weicher Röntgenemission, welche sich am gleichen Ort wie eine schalenartige Struktur befindet, die in Bildern zu sehen ist, welche mit Daten der *Magellanic Emission Line Survey* erstellt wurden. Es wird eine Spektralanalyse für die Emission innerhalb der Blasenregion durchgeführt, um den Energieinhalt dieser Blase zu bestimmen. Die Frage, ob die schalenartige Struktur zu einem Supernovaüberrest oder einer windgetriebenen Blase gehört, wird mit Hilfe der Bilder im Röntgenspektrum und dem berechneten Energieinhalt untersucht. Da der Energieinhalt relativ gering ist, im Vergleich zur möglichen Zufuhr durch massereiche Sterne, und da keine bekannten O-Klasse oder Wolf-Rayet Sterne in der Blase existieren, scheint ein Supernovaüberrest wahrscheinlich. Gleichzeitig ist es möglich, dass die Struktur zu einer windgetriebenen Blase von massereichen Sternen gehört, die später durch Supernovae von diesen Sternen gestört wurde. Da die Blase relativ alt zu sein scheint, und das Ergebnis vieler komplexer Interaktionen in ihrer Lebenszeit ist, kann keine Eindeutige Antwort gegeben werden.

Abstract

The interstellar medium (ISM) is a highly complex subject, that is generally studied by means of numerical simulations. In general the ISM can be separated into three thermal phases, a cold phase ($10 - 10^2$ K), a warm phase ($10^2 - 10^4$ K) and a hot phase ($\gtrsim 10^6$ K), that interact in a turbulent manner, forming structures like spiral arms and superbubbles. Fuelled mainly by stellar winds and supernovae, the hot phase occupies a significant fraction of the volume in the Galaxy, while on the other hand only making up less than 1% of the interstellar medium's mass. In this thesis, a bubble like structure, at the coordinates RA: $04^{\mathrm{h}}57^{\mathrm{m}}07.8^{\mathrm{s}}$ and DEC: $-69°23'58.0''$ in the Large Magellanic Cloud, is analyzed in the X-Ray spectrum, using data obtained with the XMM-Newton X-Ray observatory. While the data is heavily flare contaminated, the images clearly show a region of diffuse soft X-Ray emission, that coincides with a shell-like structure, visible in images created using data from the *Magellanic Emission Line Survey*. A spectral analysis is conducted for the emission within the bubble region, in order to determine the energy content of said bubble. The question, whether the shell-like structure belongs to a supernova remnant or a wind-driven bubble, is analyzed using the X-Ray images and the calculated energy content. With the energy content being relatively low, compared to the possible input from massive stars, and no known O-type or Wolf-Rayet stars existing within the bubble, a supernova remnant seems likely. At the same time it is possible, that the structure belongs to a wind-driven bubble from massive stars, that was later disrupted by supernovae from those stars. As the bubble appears to be relatively old, and being the result of many complex interactions over its lifetime, no definite answer can be given.

Table of Contents

List of Figures

CHAPTER 1

Introduction

When people think about astronomy or astrophysics, they normally only think about compact objects like stars. What lies in between often goes unnoticed. The space between planets and even stars is thought of as an enormous nothingness, which, with an average density of 1 particle per cubic-centimeter, is not far-fetched, but at the same time, on a cosmic scale, is vital for the evolution of the galaxies. Not only does it provide the material for star formation, in the form of dense molecular clouds, it also mediates the energy transfer from stellar winds and supernovae, needed to trigger star formation in the first place. Hence, to understand the evolution of a galaxy, is to understand the interstellar medium within.

Having a firm understanding of the ISM is easier said than done. The interstellar medium consists to 99% of gas, with 1% of the matter in the form of dust particles, but this 1% has a significant impact on what we can observe, due to dust extinction. Similarly, while hydrogen and helium make up 98% of the ISM gas, the 2% metals heavily influence the spectra of objects we observe through the interstellar medium. Determining the actual composition of the ISM proves to be quite complicated.

Besides the elemental composition, the physical parameters of the ISM, e.g. temperature and density, also have to be considered when trying to analyze its mechanics. Here we generally find the ISM in three distinct thermal phases that interact in a turbulent manner, forming structures like spiral arms, superbubbles and the galactic halo, just to name a few. The theory of the interstellar medium is normally studied, using numerical simulations, due to its complexity, while observations of actual structures, like superbubbles provide the measurement data to test the theories.

In this thesis, a structure in the Large Magellanic Cloud at the coordinates RA: $04^{\mathrm{h}}57^{\mathrm{m}}07.8^{\mathrm{s}}$ and DEC: $-69^{\circ}23'58.0''$ is studied, using X-Ray data obtained with the XMM-Newton X-Ray observatory. The X-Ray data is used to create images of the region, as well as to conduct a spec-

tral analysis of the emission. The images are compared to their optical counterparts provided by Smith et al., 2005, while the spectral data is used to determine and analyze possible source models. With the source models, the energy content of the shell-like structure is calculated, and then compared to possible energy input from massive stars. In addition, the region is compared to maps of molecular clouds and the [SII] to Hα ratio, to check for possible shocks. In conclusion the question, whether the shell-like structure belongs to a supernova remnant or a wind driven bubble, will be examined.

CHAPTER 2

The Interstellar Medium

The interstellar medium (ISM) encompasses, as the name implies, all the material and radiation between the stars in a Galaxy. It consists of all non stellar matter, radiation, magnetic fields and cosmic rays. As such, all objects outside the Solar System have to be observed through the ISM, consequently the measurements derived from such observations have to consider the interstellar medium's influence, complicating the analysis of extra-Solar objects. Observations of the ISM itself on the other hand, facilitate the study of the Galaxy's fundamental structure and its evolution.

Interstellar structures, like stellar wind bubbles and superbubbles, form through interactions with the interstellar medium, which in turn requires knowledge of the surrounding ISM to properly analyze these objects. The following sections aim to provide a basic understanding of the ISM.

2.1 ISM Composition

The interstellar medium mainly consists of hydrogen and helium, both of them together making up 98% of the ISM. While the heavier elements, referred to as metals by astronomers, only make up 2% of the ISM, they still influence the spectra of extra solar sources. For this reason, the elemental composition of the ISM, among others, is an important factor to consider in regards to spectra.

The precise mixture of elements in the interstellar medium is difficult to determine, since direct spectral measurements, as with stars, are more complicated. An additional difficulty stems from the fact, that some elements, such as carbon (C), oxygen (O), magnesium (Mg), silicon (Si) and iron (Fe), deplete from the gaseous phase into dust grains, where these elements cannot be detected through spectral features at all. Though dust only encompasses about 1% of the ISM, it acts as an efficient absorber, especially for visible light.

Since direct access to the elemental abundances is difficult, they are instead inferred, initially from solar values, and then combined with models for the dust extinction (Snow and Witt, 1996). The dust extinction is measured as a reduction in the observed flux from a well defined source. Assuming a certain total abundance for the ISM, e.g. solar, and then applying models for dust formation to the observational data of dust extinction, one is able to determine which elements deplete into dust grains, and in what quantities.

Assuming our sun to be representative of the ISM composition in general comes with some caveats. Greenberg, 1974, observed that, assuming solar abundances, the lack of heavier, dust forming elements like oxygen, carbon and nitrogen, could not be fully explained by the depletion into dust. Snow and Witt, 1996, using these discrepancies as basis, call the usage of solar abundances themselves into question.

Table 2.1 shows the mean stellar abundance values, Snow and Witt, 1996, summarized from studies of young B, F and G stars, compared to the solar values given by Anders and Grevesse, 1989. The last column holds the elemental abundances, Snow and Witt, 1996, adopted for the ISM.

They now conclude that, given the values in table 2.1, young stars in our galaxy collectively show a lower metallicity, e.g. a lower abundance for elements heavier than helium, compared to our sun. This calls into question the validity of assuming solar abundances for the ISM as a whole, for this reason Snow and Witt, 1996, based on the data from table 2.1, provide their own adopted subsolar ISM abundances. However, they run into the problem, that common dust models require more material than their modified ISM abundances provide.

The argument of Snow and Witt, 1996, for subsolar ISM abundances was based on solar values provided by Anders and Grevesse, 1989, comparing them with data from young galactic stars. In contrast, newer measurements of solar abundances as given by Asplund et al., 2009, show a drastically reduced amount of certain dust forming elements, i.e. carbon and oxygen, bringing the solar data more in line with that of young galactic stars. The problem with the shortage of dust forming elements, Snow and Witt, 1996, concluded, remains.

In a more recent work by Zuo et al., 2021, ISM abundances were calculated, using observational data of the gaseous ISM composition and dust extinction. The results were compared to the different solar and stellar values listed in table 2.2.

Protosolar abundances take the effect of sedimentation into account, where heavier elements move from the photosphere deeper into the sun. Zuo et al., 2021, conclude, based on their calculations and data, that protosolar values, including enrichment through galactic chemical evolution, are the best reference for the ISM abundances.

The ISM model components used in this work are sourced from Wilms et al., 2000, who use updated abundance values, based on the data from Anders and Grevesse, 1989.

Table 2.1. Comparison of solar abundances with stellar abundances from different stars, given by Snow and Witt, 1996. All values are given relative to 10^6 H-atoms.

Element	Sun[a]	Field B Stars[b]	Cluster B Stars[b]	Disk F, G Stars[c]	Adopted ISM Value
C	363	204	224	209	214
N	112	67.6	63.1	···	66
O	851	380	490	490	457
Mg	38.0	23.4	20.9	30.2	25
Si	35.5	15.8	15.8	24.0	18.6
S	16.2	11.7	12.9	···	12.3
Ca	2.29	1.70	···	1.45	1.58
Ti	0.10	0.06	···	0.07	0.065
Cr	0.47	0.32	···	···	0.32
Fe	46.8	30.9	32.4	18.2	26.9
Ni	1.78	1.15	···	1.07	1.12

Note. — (a) Solar abundances by Anders and Grevesse, 1989; (b) B-star abundances by Kilian, 1994, Adelman et al., 1993 and Gies and Lambert, 1992; (c) Disk F, G Star abundances by Edvardsson et al., 1993 and Tomkin et al., 1995.

Table 2.2. Comparison of solar, stellar and protosolar abundances for main elements in dust formation from Zuo et al., 2021. All values are given relative to 10^6 H-atoms.

Element	B-stars[a]	Solar[b]	Solar[c]	Protosolar[d]	Protosolar with GCE[e]
C	209 ± 15	363 ± 33	269 ± 31	288 ± 27	339 ± 39
O	575 ± 40	851 ± 69	490 ± 57	575 ± 66	589 ± 68
Mg	36.3 ± 4.2	38.0 ± 4.4	39.8 ± 3.7	41.7 ± 1.9	47.9 ± 4.4
Si	31.6 ± 1.5	35.5 ± 4.1	32.4 ± 2.2	40.7 ± 1.9	42.7 ± 4.0
Fe	27.5 ± 2.5	46.8 ± 3.2	31.6 ± 2.9	34.7 ± 2.4	47.9 ± 4.4

Note. — (a) B-star abundances by Przybilla et al., 2008; (b) Solar abundances by Anders and Grevesse, 1989; (c) Solar abundances by Asplund et al., 2009; (d) Protosolar abundances by Lodders, 2003; (e) Protosolar abundances with Galactic-Chemical-Evolution (GCE) by Asplund et al., 2009 and Chiappini et al., 2003.

2.2 ISM Morphology and Star Formation

The interstellar medium is a complicated concept. Something as simple as the composition, i.e. the elements it consists of, is already difficult to describe. Modeling the ISM as a whole subsequently also proves to be an extremely demanding task. It should be obvious, that the properties of the ISM highly depend on the location, within the galaxy, that we observe.

From the galactic disk to the halo, from hot stellar bubbles and supernova remnants to cold neutral hydrogen clouds, the specific characteristics of the ISM will be considerably different. Still, on large enough scales it is useful to attempt to create a general model for the interstellar medium, since the ISM has to be considered in all research of extra solar targets. Parameters in this general model can then be adapted to account for regional differences where necessary.

While early models, due to the lack of computing power, were limited in their ability to consider all of the factors influencing the ISM, modern technology allows for more precise and extensive simulations, incorporating many more parameters. One result of such a simulation can be seen in figure 2.1 from a work by Hopkins et al., 2012, where models for different galaxy types were simulated on a galactic scale.

An important part of the simulation work by Hopkins et al., 2012, was to analyze the effects different feedback mechanisms have on the ISM. Without stellar feedback, e.g winds or super novae, the gas concentrated in giant molecular clouds (GMC) would undergo a runaway collapse, turning up to 100% of the gas into stars. This effect extends to the whole galaxy, as the ISM would rapidly cool, feeding an explosive star formation that would lead to more stars than we can observe.

Turbulence or purely thermal pressure is insufficient to halt the ISM collapse, as the cooling would eliminate the thermal pressure and turbulences would dissipate within a single crossing time.

In practice a multitude of stellar mechanisms like radiation pressure and super novae, among many others, provide feedback that counteracts the runaway collapse. Some effects can even cause material to be expelled from the galaxy. The extensive list of possible feedback sources makes comprehensive simulations difficult. The physical mechanisms explicitly considered by Hopkins et al., 2012, include the following:

- Star formation and molecular gas
- Gas cooling
- Mass recycling through stellar winds and super novae
- Radiation pressure
- Energy/momentum transfer from stellar winds and from super novae

- HII Photoionization

Figure 2.1 shows the simulation results for two Milky Way models after about two orbital periods, when the system reached a feedback controlled steady state. The images display the resulting morphology with a mock u/g/r observation in the top row and a gas/temperature distribution in the bottom row.

For both image types and Milky Way models a top- and side-on view are given. In the bottom row, the temperature distribution is given as three components, with cold ($\lesssim 1000$) molecular gas in blue, warm ($T \sim 10^4 - 10^5$ K) ionized gas in pink and hot ($T \gtrsim 10^6$ K) gas in yellow. The left set of images displays a Milky Way model with a higher dark matter fraction than actually assumed, which leads to the lack of a central bar, while still forming the canonical spiral arms. The model on the right side shows a clear barred-spiral structure, with most of the cold and warm gas concentrated in the central bar and spiral arms combined with a halo of hot gas. Star formation is concentrated in stellar clusters, visible as small blue knots in the spiral arms and the bar. In the disc we can also clearly see bubbles in the form of holes.

In figure 2.2 Hopkins et al., 2012, displays the star formation history (SFH) of the four galaxy models they simulated, a high-redshift massive starburst disc (HiZ), a luminous-infrared galaxy (Sbc), a Milky Way like galaxy and a Small Magellanic Cloud dwarf galaxy (SMC). In the following, the focus will lie on the Milky Way model.

For each galaxy type, the SFH is plotted with different feedback mechanisms turned on and off. Without any feedback enabled (dashed purple line), a large part of the gas collapses into giant molecular clouds (GMC) within a single dynamical time (average orbital time), which leads to rapid star formation with a peak star formation rate (SFR) of $40\,M_\odot yr^{-1}$ for the Milky Way model.

The later decline in SFR is solely explained by gas depletion. With all feedback activated, the MW model reaches a quasi-steady equilibrium, which holds for many dynamical times, while maintaining a SFR between $1 - 2\,M_\odot yr^{-1}$.

In the MW model, local momentum deposition and long range radiation pressure show to have the strongest effect on star formation history, with heating through super novae also having the highest impact on heating the ISM.

2.3 The three phase Interstellar Medium

A common principle in modern ISM models is the separation into three thermal components, see Sasaki et al., 2022, and references therein:

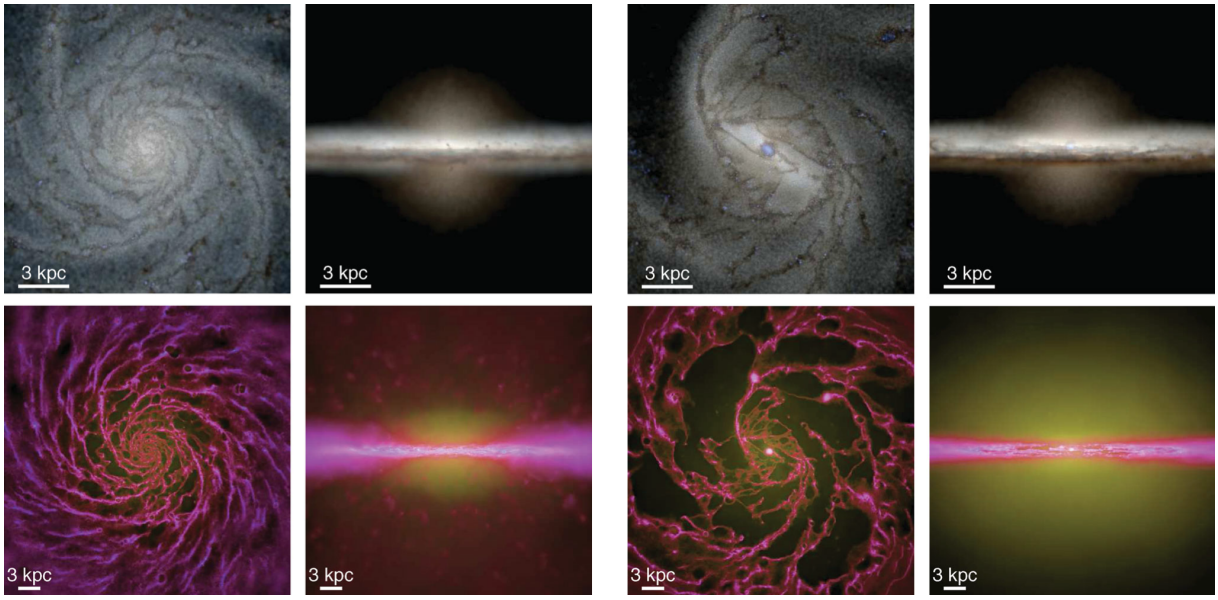

Figure 2.1: Morphological results from a galaxy spanning simulation by Hopkins et al., 2012. The two sets of images show the morphology of the Milky Way model with a higher dark matter content (left) and the canonical dark matter content for our galaxy (right). The upper row depicts a mock u/g/r composite observation of the stellar distribution, while the bottom row shows gas density via intensity and temperature via color. Blue for $T \lesssim 1000\,\mathrm{K}$ molecular gas, pink for $T \sim 10^4 - 10^5\,\mathrm{K}$ ionized warm gas and yellow for $T \gtrsim 10^6\,\mathrm{K}$ hot gas. For each dark matter content and image type, a face-on and edge-on view is given. The images are created when the disc reaches a feedback controlled steady state, after evolving through approximately 2 orbital periods. The Milky Way model with a higher dark matter fraction doesn't develop a bar, but still forms spirals containing dust lanes, and becoming spurred at the outer reaches. Star formation mainly occurs in clusters, visible as small blue knots within the spiral arms. The bar-spiraled morphology on the right shows an even more distinct concentration of gas in the spirals with increased star cluster formation within the bar. (Adapted from fig. 3 and fig. 4 in Hopkins et al., 2012, ©the authors)

- A cold atomic/molecular phase with temperature $T \sim 10 - 10^2\,\mathrm{K}$, high density $n \sim 10^2 - 10^5\,\mathrm{cm}^{-3}$ and low filling factor
- A warm neutral/ionized phase with temperature $T \sim 10^2 - 10^4\,\mathrm{K}$, density $n \sim 10^{-1} - 10\,\mathrm{cm}^{-3}$ and a significant filling factor in the mid-plane
- A hot ionized phase with temperature $T \gtrsim 10^6\,\mathrm{K}$, density $n \lesssim 10^{-2}\,\mathrm{cm}^{-3}$ and a large, but unknown filling factor

Besides the thermal phases, the gas component of the ISM can also be classified by its atomic state, i.e. molecular, atomic/neutral and ionized. These atomic states strongly correlate with the temperature, as can be seen in the list above. The cold gas exists as a mixture of neutral

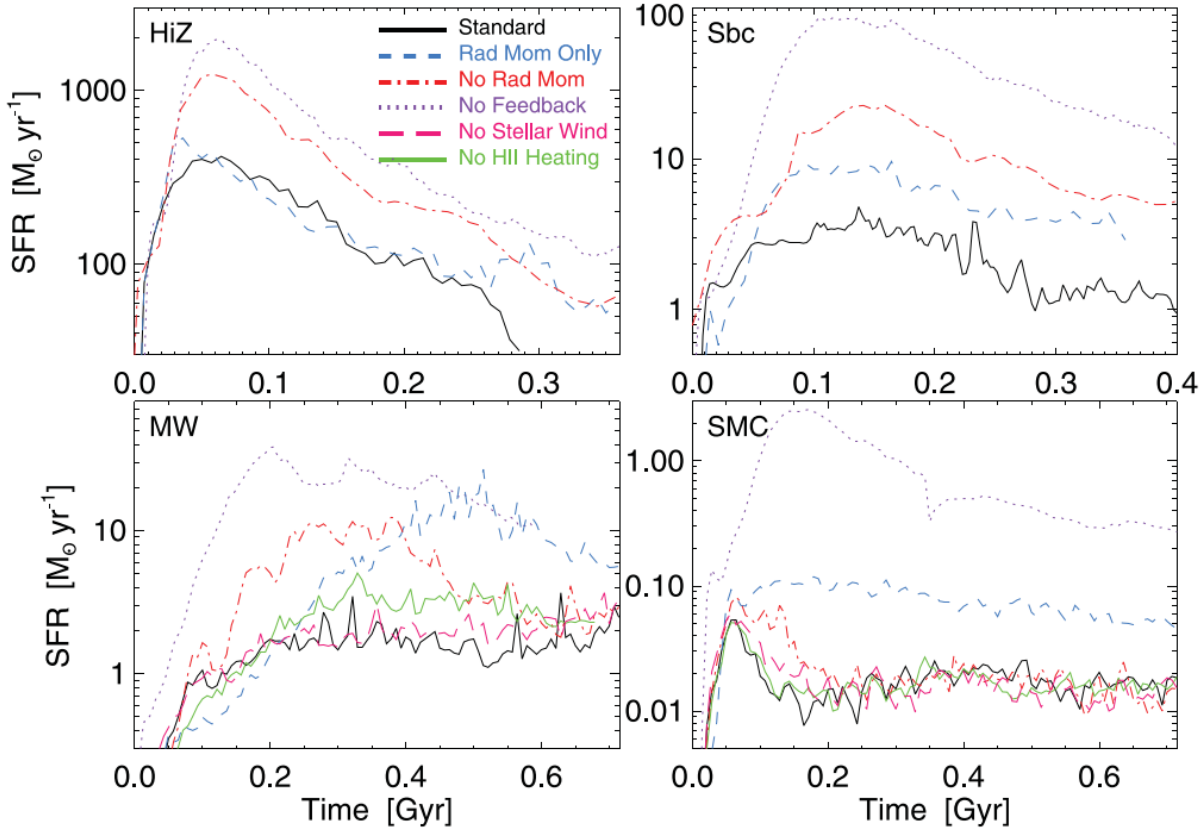

Figure 2.2: Star formation histories obtained from the simulation by Hopkins et al., 2012, for four different galaxy models, a high-redshift massive starburst disc (HiZ), a luminous-infrared galaxy (Sbc), a Milky Way like galaxy (MW) and a Small Magellanic Cloud dwarf galaxy (SMC). For each model, the star formation rate (SFR) is plotted over the simulated age of the galaxy, with different feedback mechanisms switched on and off. Without any feedback (purple dotted line), all galaxies show runaway collapse, resulting in rapid star formation in the early ages, followed by a steady drop, as the gas is depleted. With all feedback enabled (solid black line), the MW and SMC reach a quasi-steady equilibrium, while the HiZ and Sbc model still show a decline in SFR, due to gas depletion. (Adapted from fig. 7 in Hopkins et al., 2012, ©the authors)

and molecular states, while the hot gas is completely ionized and the warm gas transitions from ionized to neutral.

Figure 2.3 shows the column densities of different ISM components, including cosmic rays and magnetic fields, as well as the temperature obtained from a simulation of the interstellar medium by Rathjen et al., 2021. The image shows the state of the simulation after 65 Myr evolution as a side-on view in the upper and a top-on view in the bottom row. White circles in the first and third column represent star clusters scaled to their masses, with transparent circles representing old star clusters without active massive stars.

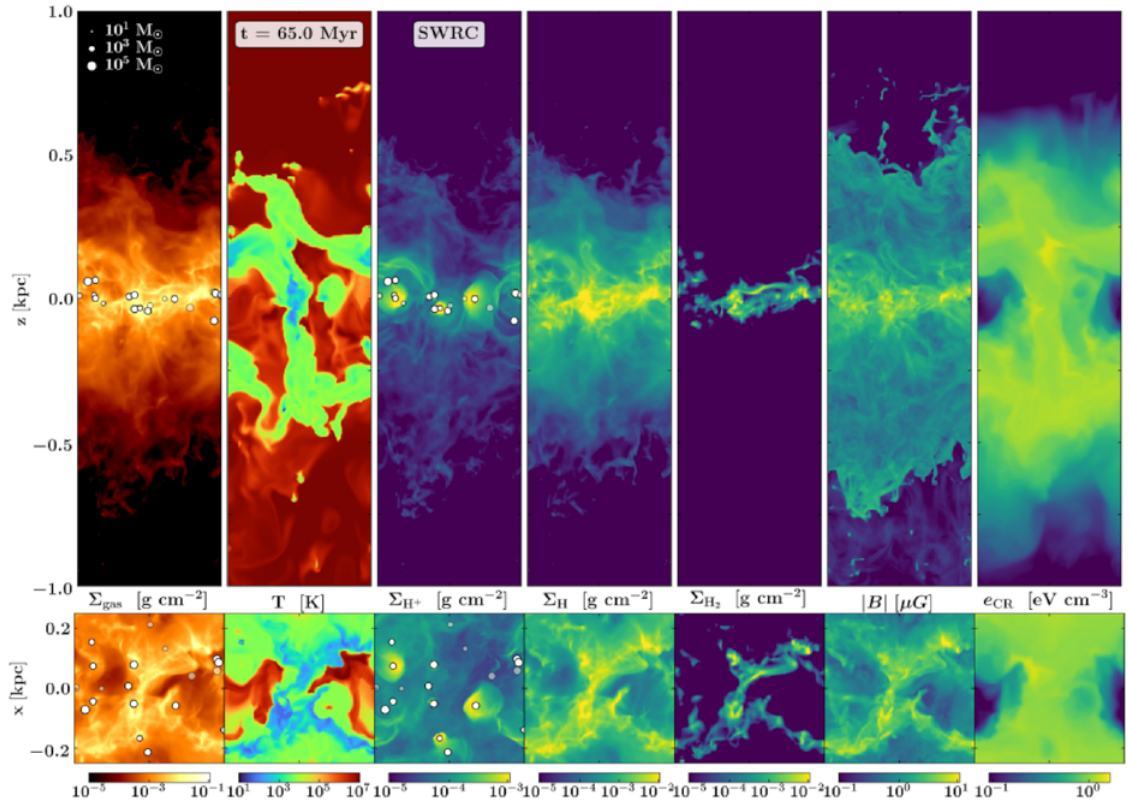

Figure 2.3: Results from a multi-phase ISM simulation by Rathjen et al., 2021. The image shows the column densities for different components of the ISM, obtained in the simulation. From left to right, the panels show total gas, temperature, ionized-, atomic-, and molecular hydrogen as well as magnetic field strength and cosmic ray energy density in the last two panels. The small white circles in panels 1 and 3 represent star clusters of different masses, with the translucent ones being older clusters with no active massive stars. (Adapted from Fig. 1 in Rathjen et al., 2021, ©the authors)

Hopkins et al., 2012, also analyzed different phases of the ISM in their simulation. The results for three models, the high-redshift massive starburst disc (HiZ), the Milky Way like galaxy (MW) and the Small Magellanic Cloud dwarf galaxy (SMC), with all feedback enabled, are displayed in figure 2.4. The first two rows plot the mass-weighted probability density function (PDF) for the density of the gas in the ISM ($\mathrm{d}m/\mathrm{d}\log n$). For the plots in the top row, the density distribution was separated into the following three components:

- Star forming disc
  Defined as the volume of gas, which is both within one vertical scale height, and the radius encompassing 50% of star formation.

- Wind
  Defined as gas beyond one scale height, with radial velocity $v_r > 100\,\mathrm{km\,s^{-1}}$, and radial velocity ratio $\frac{v_r}{|v|} \geq 0.75$.

- HI-disc and halo
  Defined as gas between star forming disc and wind.

The total gas density distribution (black dashed line) has a wide dynamic range that cannot be compared to available ISM density studies.

For the MW-like model the star forming disc (blue dashed line) reaches up to 10 kpc, and encompasses nearly all gas with a density $n \gtrsim 1\,\mathrm{cm^{-3}}$. The wind (solid orange line) holds the largest fraction of hot gas, with temperatures $T \gtrsim 10^6\,\mathrm{K}$ and very low densities, in part due to the simulation not containing intergalactic medium, which allows for arbitrarily low densities to develop.

A large fraction of the total gas finds itself in the extended disc and halo (dashed green line), which include gas of intermediate densities. This comprises the initial extended gas disc with low density ionized hydrogen ($T_{\mathrm{eff}} \sim 10^5\,\mathrm{K}$), as well as material expelled by feedback from the star forming disc, which lacks the energy/momentum to form an outflow.

For the plots in the middle and bottom row Hopkins et al., 2012, separates the gas in the star forming disk (see top row) into the three thermal phases as follows:

- Cold atomic and molecular gas with $T < 2000\,\mathrm{K}$
- warm ionized gas with $2000\,\mathrm{K} < T < 4 \times 10^5\,\mathrm{K}$
- hot ionized gas with $T > 4 \times 10^5\,\mathrm{K}$

From the plots in figure 2.4 one can gather, that high density gas with $n > 1\,\mathrm{cm^{-3}}$ is mostly cold, that gas with densities n between $0.01 - 1\,\mathrm{cm^{-3}}$ is warm and that hot gas has densities $n < 0.01\,\mathrm{cm^{-3}}$. Cold gas holds the largest mass fraction, followed closely by the warm phase, with hot gas making up only a few percent ($1 - 3\%$) of the total gas mass. The density distribution of the total gas and its components can be considered to be roughly log-normal.

The bottom row shows the volume-weighted density distribution ($\mathrm{d}V/\mathrm{d}\log n$) for the above listed phases in the star forming disc. Regarding volume, the hot phase holds a filling factor $f_{\mathrm{h}} \sim 1$, with the warm phase still occupying a significant fraction having a filling factor $f_{\mathrm{w}} \sim 0.5$ for the MW-model. The warm gas is mainly concentrated in denser structures like spiral arms and shells. In contrast to its mass, the cold gas only has a filling factor $f_{\mathrm{c}} \sim 1 - 3\%$.

In a more recent simulation Rathjen et al., 2021, also analyzed the ISM and in particular its different phases. Similar to Hopkins et al., 2012, Rathjen et al., 2021, likewise ran multiple simulations for different feedback mechanisms, starting with only supernova explosions (S), then

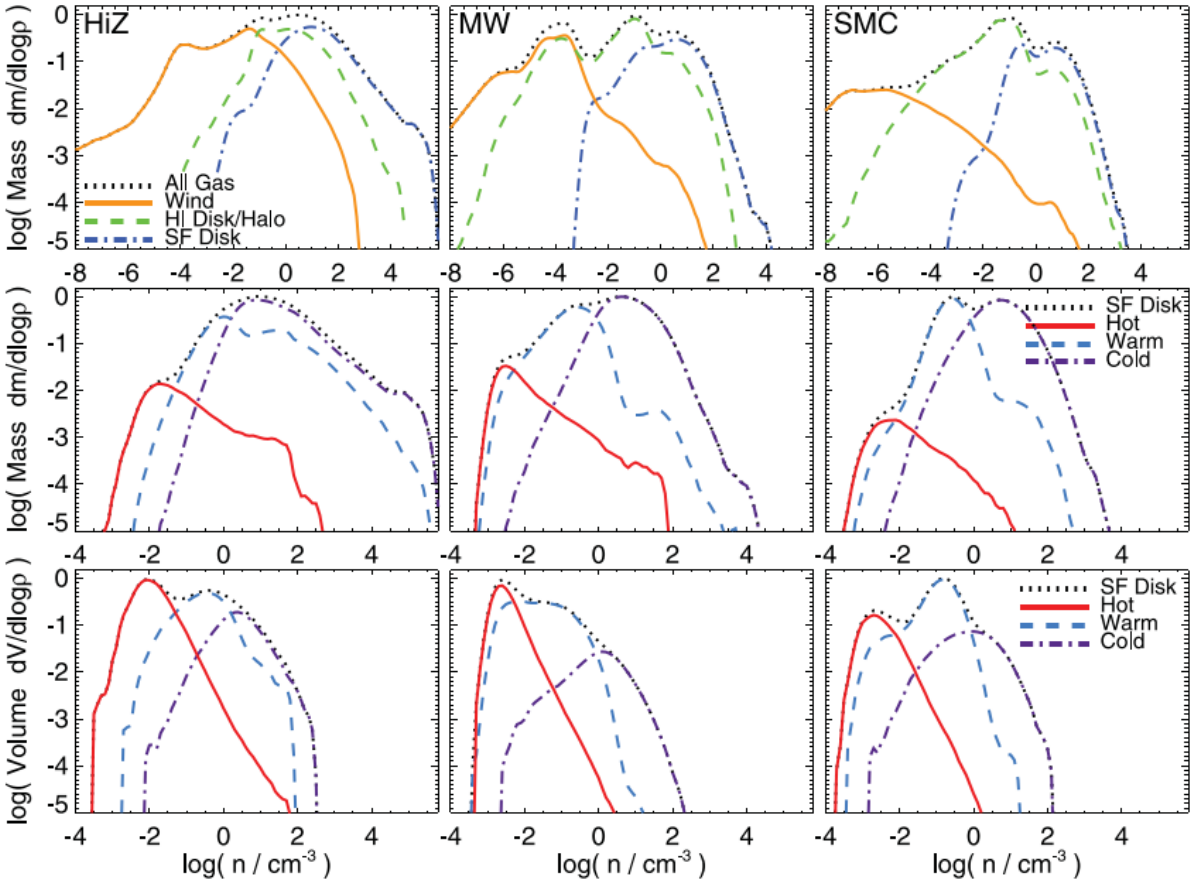

Figure 2.4: Depicted here are the density distributions for different phases of the ISM in three of the galaxy models, namely the HiZ, MW and SMC, from the simulation by Hopkins et al., 2012 (see 2.2). All models had reached a feedback regulated steady state for the plots. The top two rows display the mass-weighted density PDF for different regions in the model (top) and the thermal phases (middle). The bottom row displays the volume-weighted density PDF for the different thermal phases. (Adapted from fig. 11 in Hopkins et al., 2012, ©the authors)

adding stellar winds (SW), ionizing radiation (SR and SWR) and finally cosmic rays (SWC and SWCR).

Each simulation run covers a time frame of 100 Myr but, unlike Hopkins et al., 2012, is spatially limited and does not extend to the whole galaxy. Figure 2.3 shows the visualized simulation results for the SWCR run, which includes all feedback mechanisms. At a simulated age of 65 Myr, different elements and parameters of the ISM are depicted.

The column densities for ionized (H^+), neutral (H) and molecular (H_2) hydrogen appear in panels three, four and five respectively, with the total gas column density being shown in the first panel. The temperature distribution is visible in the second panel and the magnetic field

and cosmic ray energy density are depicted in panels six and seven each. The upper row gives an edge-on and the bottom row a top-on view, with the white circles in panel one and three depicting stellar clusters. The circle radii are proportional to the cluster mass, while translucent circles represent old clusters with no active massive stars.

Rathjen et al., 2021, also investigated the structure of the ISM in regards to the three thermal phases, cold ($T \leq 300\,\mathrm{K}$), warm ($T \leq 3 \times 10^5\,\mathrm{K}$) and hot ($T > 3 \times 10^5\,\mathrm{K}$). To this end they averaged the volume-filling factors (VFF) and mass fractions (MF) of the different ISM phases within the galactic midplane ($z = \pm 250\,\mathrm{pc}$) between 25 Myr and 100 Myr. The resulting values for the VFF and MF of the ISM phases can be found in tables 2.3 and 2.4 with the warm phase further separated into an ionized and neutral phase. The averaged VFF and MF values are calculated separately for each simulation run with different feedback mechanisms. In addition to the simulation results, observational estimates for the solar neighborhood from Tielens, 2005, are given for comparison. A visual representation of the results is provided in figure 2.5.

In the simulation with supernova explosions as sole feedback mechanism (S), hot gas, as one would expect, dominates with a volume-filling factor $\sim$ 90%. The introduction of winds and cosmic rays (SWC) results in an VFF increase of warm gas by about 25 per cent points, including 6% collisionally ionized gas. Ionizing radiation in the SR, SWR and SWRC runs has the most significant impact on the volume filling factor of warm and hot gas, causing a decrease of $\mathrm{VFF_{hot}}$ to 35-55%, with a corresponding increase of $\mathrm{VFF_{warm}}$. This additional warm and neutral gas originates from HII regions through recombination.

The mass fractions (MF) show a more or less opposite behavior, with cold gas acting as the dominant phase for simulation runs without ionizing radiation. In the SR, SWR and SWRC run including radiation, one can see an increase of $\mathrm{MF_{warm}}$ by $\sim$ 20 per cent points, this time with a corresponding decrease for the mass fraction of cold gas, due to heating from massive stars. In the case of the mass fractions, stellar winds provide no significant impact on the thermal ISM phases.

2.4 Sources of the Hot Interstellar Medium

While far- and extreme-ultra violet radiation (FUV, EUV) is able to heat cold gas and transfer it to the warm phase, transition to the hot phase usually requires strong shocks.

An adiabatic shock, at a velocity v_{sh}, reaches a post-shock temperature of

$$T_{ps} = \frac{3\mu}{16k} v_{sh}^2 = 1.4 \times 10^7\,\mathrm{K} \left(\frac{v_{sh}}{1000\,\mathrm{kms}^{-1}} \right)^2 , \tag{2.4.1}$$

for a plasma with common ISM abundances, an adiabatic index $\gamma = 5/3$, and an average particle mass 1.0×10^{-24} g (see Sasaki et al., 2022, and references therein).

Table 2.3. Comparison of volume-filling factors (VFF) for the different thermal ISM phases from Rathjen et al., 2021, and observational estimates for the solar neighborhood from Tielens, 2005. All values are given as per cent.

Enabled feedback	VFF_{hot}	$VFF_{warm}{}^{ionized}$	$VFF_{warm}{}^{neutral}$	VFF_{cold}
S	89 ± 10	2 ± 2	7 ± 7	1 ± 1
SW	82 ± 7	4 ± 2	12 ± 6	2 ± 1
SWC	73 ± 6	6 ± 2	19 ± 5	2 ± 1
SR	56 ± 16	11 ± 7	30 ± 10	2 ± 1
SWR	53 ± 16	13 ± 9	32 ± 9	2 ± 1
SWRC	35 ± 26	14 ± 7	50 ± 21	2 ± 1
Tielens	~ 50	25	30	1.05

Table 2.4. Comparison of mass fractions (MF) for the different thermal ISM phases from Rathjen et al., 2021, and observational estimates for the solar neighborhood from Tielens, 2005. All values are given as per cent.

Enabled feedback	MF_{hot}	$MF_{warm}{}^{ionized}$	$MF_{warm}{}^{neutral}$	MF_{cold}
S	0.4 ± 0.3	2 ± 1	27 ± 7	71 ± 7
SW	0.2 ± 0.1	1.4 ± 0.4	28 ± 6	70 ± 6
SWC	0.2 ± 0.1	1.6 ± 0.5	34 ± 4	64 ± 4
SR	0.05 ± 0.02	8 ± 5	45 ± 12	47 ± 14
SWR	0.04 ± 0.01	8 ± 5	43 ± 8	50 ± 11
SWRC	0.03 ± 0.01	6 ± 3	48 ± 11	46 ± 13
Tielens	N.A.	14	38	48

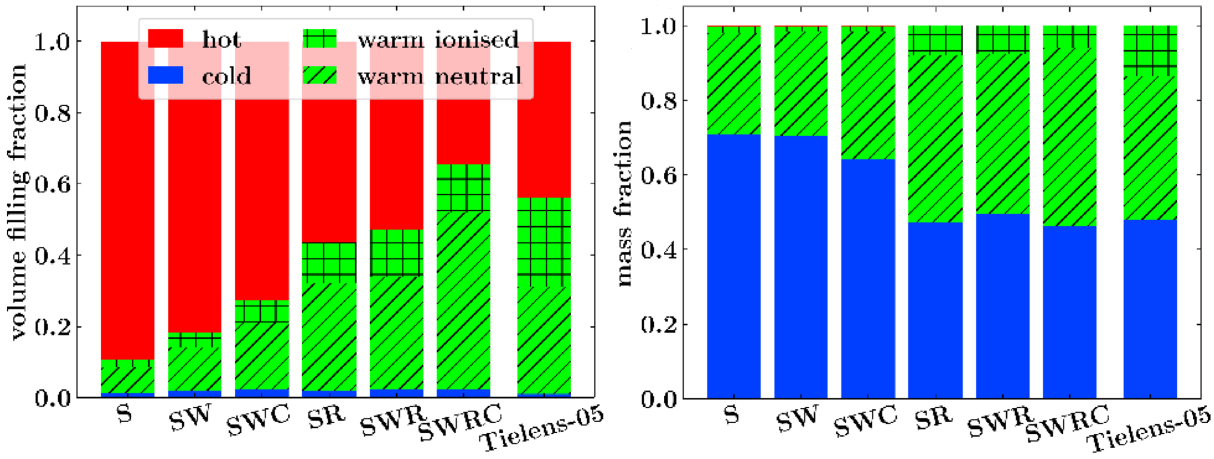

Figure 2.5: The image shows the volume-filling factors (VFF) and mass fractions (MF) of the different ISM phases for the six simulation runs by Rathjen et al., 2021, and the observational estimates from Tielens, 2005. The values for each run were averaged over the time between 25 Myr and 100 Myr. In the simulation with SNe as sole feedback mechanism (S), hot gas ($T > 3 \times 10^5$ K) dominates the volume with a VFF $\sim$ 90%. Adding radiation (SR, SWR and SWRC) significantly increases the VFF of warm gas ($T > 300$ K) and increases the fraction of ionized warm gas due to photo-ionization. In the case of mass fraction, radiation feedback lowers the MF of cold gas ($T < 300$ K), in turn increasing the warm gas MF by $\sim$ 20 per cent points. (Adapted from fig. 11 in Rathjen et al., 2021, ©the authors)

Shocks of velocities $v_{sh} \lesssim 1000\,\mathrm{kms}^{-1}$ within the cold/warm gas radiate energy very efficiently, and therefore cannot add gas to the hot phase. Shock velocities above $1500\,\mathrm{kms}^{-1}$ correspond to a post-shock temperature $T_{ps} \sim 3 \times 10^7$ K, at which the only remaining effective mechanism for cooling is bremsstrahlung.

For an electron number density n_e, we find the cooling rate $\dot{E} \propto n_e^2\sqrt{T}$,which translates to a cooling timescale $t_c = \frac{E}{\dot{E}} \propto n_e^{-1}\sqrt{T}$ that increases with temperature. Typical values range between $10^6 - 19^9$ yr for temperatures $T \gtrsim 3 \times 10^7$ K, see Sutherland and Dopita, 1993.

Shocks with speeds $v_{sh} \gtrsim 1500\,\mathrm{kms}^{-1}$ predominantly originate from supernovae and stellar winds from massive stars, e.g. O/B-stars and Wolf-Rayet stars. In a lesser capacity, winds from low-mass stars, novae and proto-stellar jets can heat gas to temperatures $T > 10^6$ K.

While objects like pulsar-wind nebulae, high-mass X-Ray binaries and microquasars also produce hot gas in the ISM, their overall energy input is insignificant compared so SNes and stellar winds. Their accumulated energy and matter input form large scale structures like supperbubbles and Galactic fountains, which in turn pose as the dominant source for the hot phase of the ISM and its dynamics.

Although these large structures make easy targets for observation, due to their high amount of emission, the actual interpretation of the gathered data is substantially complicated by the complex history and unknown initial conditions of these structures.

ISM observations around hot stars reveal a gas temperature $T \approx [1-3] \times 10^6\,\mathrm{K}$, which is significantly lower than the temperature predicted by equation 2.4.1. This implies turbulent mixing or thermal conduction of denser gas at the shock interface, which in turn leads to energy losses in the hot gas, see Toalá and Arthur, 2018.

The low density hot gas ($T \sim 10^7$) K within supernova remnants is a significant source of soft X-Ray emission. Hence, analyzing the SNR population in its entirety is necessary to fully grasp the interactions and properties of the different ISM phases, see Sasaki et al., 2022.

2.5 The Magellanic Clouds

A major obstacle in observing soft X-Ray emission lies within the easy absorption of these X-Rays by interstellar matter, making it difficult to study this emission within the Milky Way.

An alternative avenue to study the hot phase of the ISM through soft X-Rays presents itself in the form of the Magellanic Clouds. The Small- and Large-Magellanic Cloud (SMC and LMC) are positioned well above the galactic plane, suffering far less from fore-ground absorption, and both the LMC and SMC are comparatively close, with distances of 50 kpc and 60 kpc respectively, see Sasaki et al., 2022.

Extensive studies of SNR populations in the Magellanic Clouds have resulted in $\sim$ 60 confirmed supernova remnants in the LMC, with a long list of candidates, see Yew et al., 2021, and Bozzetto et al., 2017.

With the total stellar mass of the Milky Way ($6 \times 10^{10}\,\mathrm{M}_\odot$) being 20 times larger than that of the LMC ($2.7 \times 10^9\,\mathrm{M}_\odot$), one would expect an increase of supernova remnants by at least one order of magnitude. This means, comparing the 60 confirmed SNRs in the LMC to the 300 known SNRs and candidates in the Milky Way, the sample in the LMC is more complete, see Sasaki et al., 2022.

CHAPTER 3

Data Analysis

3.1 XMM Data

The X-ray data used for the following analysis originates from the XMM-Newton observation with the Obs-ID: 0841660301. The observation was carried out between 2020.04.11 21:37:57 and 2020-04-12 13:14:46, for a total duration of 56.21 ks, following a proposal (ID 084166) by Dr. Patrick Kavanagh, submitted during the 18th XMM-Newton announcement of opportunity.

The stated goal of the proposal was the observation of SNR candidates in the LMC with multi-wavelength signatures, but no confirmed X-ray counterpart. The observation targeted the coordinates RA: $04^{h}57^{m}07.8^{s}$ and DEC: $-69°23'58.0''$. The quality report indicates a significant amount of flare contamination, with 27.0% and 24.5% flaring, with the MOS1 and MOS2 detectors respectively, and 49.0% with the PN detector.

3.2 The XMM-Newton observatory

The X-Ray Multi-Mirror (XMM)-Newton astronomy mission was proposed to the European Space Agency (ESA) in November 1982, as a successor to ESA's European X-Ray Observatory satellite (EXOSAT), which operated between 1983 and 1986. Two large European X-Ray satellite missions ran between EXOSAT and XMM, ROSAT, a German-British mission, from 1990 to 1999, and BeppoSAX, a Italian-Dutch mission, from 1996 to 2002. For reference see Schartel et al., 2022, and the references therein.

XMM-Newton required significant technological innovation, in order to be able to fulfill its scientific goals. The spacecraft carries three telescopes together with three corresponding detectors, two MOS-type CCDs and one pn-typ CCD. Two Reflection Grating Spectrometers (RGS) are placed between the two MOS CCDs and their respective telescopes. Together, the three

cameras, the two MOS-type and the one pn-type, form the European Photon Imaging Camera (EPIC). In addition to its X-Ray detectors, XMM-Newton also features an optical monitor, see Schartel et al., 2022.

Figure 3.1 shows, on the left side, a technical drawing of the observatory, with the EPIC module being part of the Focal Plane Assembly (FPA). On the right side is a picture of the XMM-Newton Flight Model, after acoustic testing at the European Space Research and Technology Centre (ESTEC).

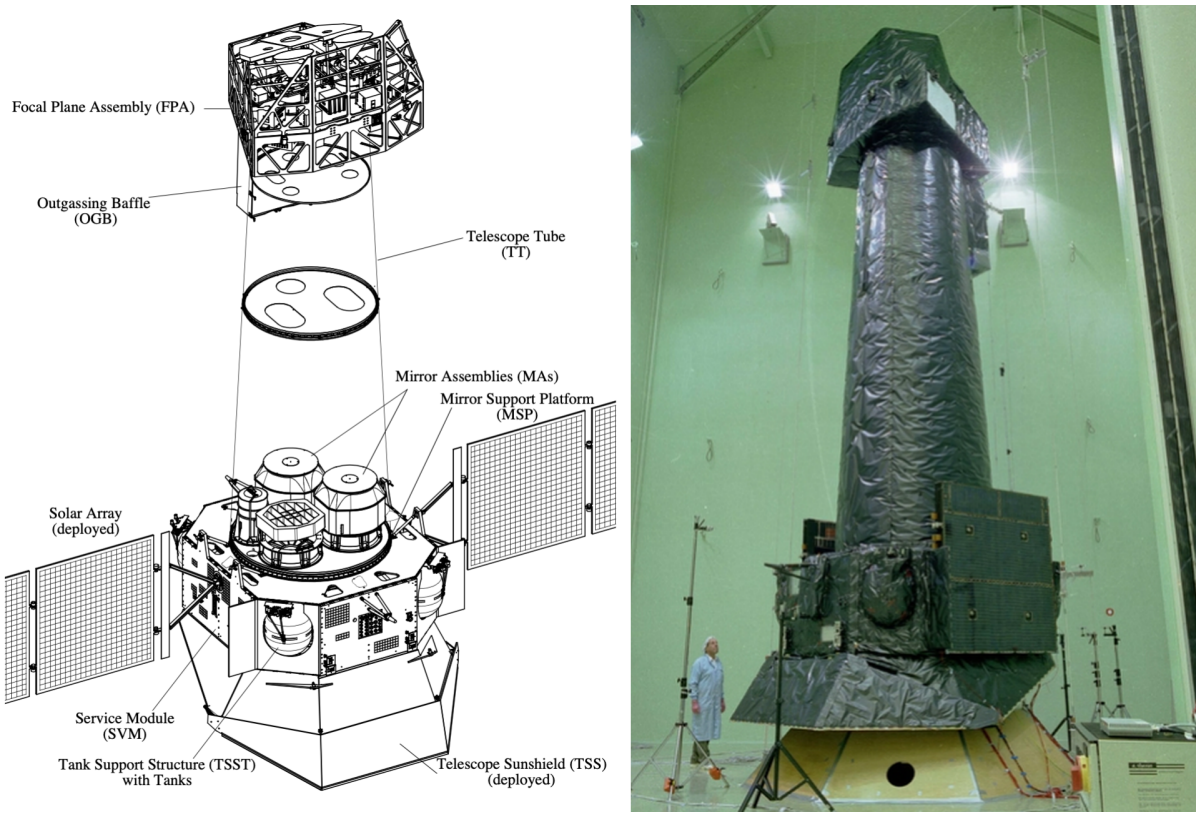

Figure 3.1: Images showing the XMM-Newton observatory. On the left side, a technical schematic of XMM-Newton is depicted, on the right a picture of the XMM-Newton Flight Model spacecraft. (Adapted from fig. 1 and fig. 2 in Schartel et al., 2022, ©the authors)

The XMM-Newton observatory was launched onboard an Ariane V rocket on December 10, 1999, and placed in a highly eccentric orbit, with a $\sim$ 48 hour period. In order to facilitate passive cooling of the X-Ray instruments to between -80° C and -100° C, an apogee of 11400 km and a perigee of 7000 km with 40° inclination was chosen. Since parts of the orbit lie within the radiation belts, operations are only conducted at altitudes $\geq$ 60000 km, see Jansen et al., 2001.

The spacecraft of XMM-Newton features a pointing accuracy of one arcsec with three-axis stabilization. Energy is provided by a 1.8 kW solar array in conjunction with two nickel-cadmium

batteries. XMM-Newton requires a permanent direct connection to ground control, since no onboard data storage and very little automation is in place. In 2008 the mission had to be recovered after a 5 day long loss of contact, due to a faulty RF subsystem antenna switch. In 2013 a fourth back-up reaction wheel was activated, halving the fuel consumption, see Schartel et al., 2022.

The three telescopes of XMM-Newton are constructed from 58 Wolter I grazing-incidence mirrors placed in a nested, coaxial and confocal arrangement, see figure 3.2. The main objective of the design was to achieve as large an effective area as possible within the energy range of 0.2–12 keV. This goal required a very small grazing angle of 30′, resulting in a focal length of 7.5 m. The diameter of the largest mirrors, limited by the shroud of the launcher, amounts to 70 cm.

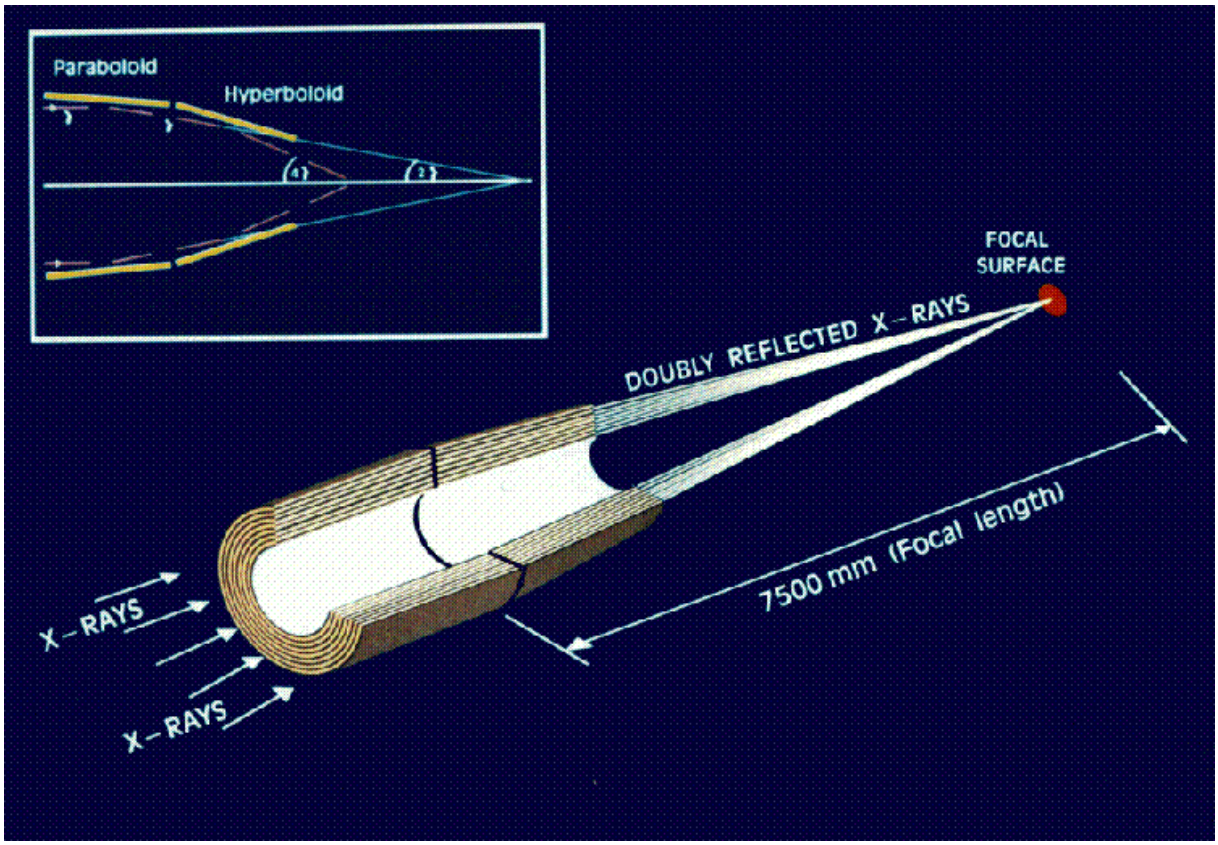

Figure 3.2: Schematic depiction of the X-Ray light path within the XMM-Newton Wolter I telescope assembly. (Adapted from fig. 2 in Dahlem, 2023, ©the authors)

An electron deflector placed at the exit aperture side of the telescopes, uses a circumferential magnetic field to deflect electrons, reflected by the mirrors, and prevents them from reaching the detectors in the focal plane. X-Ray baffles, placed in front of the telescopes, act as collimators, significantly limiting the amount of stray light reaching the focal plane instruments.

The EPIC module is capable of performing imaging and spectroscopy tasks over a 30′ field-of-view within a 0.15−15 keV energy range. The angular resolution is set by the 6″ FWHM diameter of the point-spread-function (PSF). Spectroscopy can be conducted with a moderate energy resolution of $E/\Delta E \sim 20 - 50$. Since the launch of XMM-Newton, multiple micrometeorite impacts have occurred, two of which caused the loss of CCD modules 3 and 6 of the MOS 1 detector, see Schartel et al., 2022.

3.3 Data extraction

The data was extracted, following the manual provided by Snowden and Kuntz, 2024, for the XMMSAS software version 20.0.0. The flowchart in figure 3.3 lists, in order, all the necessary tasks for the extraction of spectra and image production. The tasks in the top section are required for both spectra, and images, while the bottom section contains tasks, only required for image production.

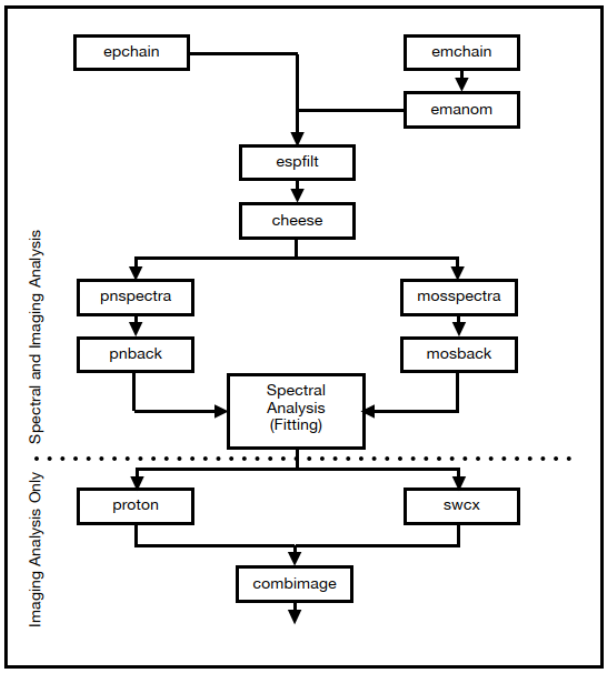

Figure 3.3: Task flowchart for the data extraction following the ESAS manual provided by Snowden and Kuntz, 2024. Extraction of spectra requires only the upper part, while image production requires both upper and lower part of the flowchart. (Adapted from Fig. 5 in Snowden and Kuntz, 2024, ©the authors)

As the first step, the chain commands, i.e. *emchain* and *epchain*, are called to create event files from the raw data. A first check of the resulting event files showed, that ccd 3 and ccd 6 in the

MOS1 detector were non functional and thus had to be excluded from the extraction. The next step comprises the soft proton (SP) filtering using the *espfilt* task, which creates a 2.5-8.5 keV light curve each, for the field-of-view (FOV) and corner data. In addition to the light curves, a count rate histogram for the FOV-data is created. The light curves and histograms are shown in figure 3.4.

The *espfilt* task then proceeds with a Gaussian-fit (green curve) of the count rate histograms for each instrument, from which the 1.5σ threshold is determined, that is used to filter the soft protons. The green areas in the light curves show the accepted sections, with the remaining white sections being filtered out.

With the count rate threshold from the histogram fit, *espfilt* automatically generates a good-time-interval (GTI) file, which is used in the further data extraction to exclude the SP - contamination. The light curves in figure 3.4 clearly present themselves heavily contaminated by soft protons, with the PN-detector most heavily affected. As not to limit the available data too significantly, a manual GTI file was created, in which only events after 43 ks were removed. The manually created GTI file was only used for the spectral extraction, while image creation proceeded with the GTI file from the *espfilt* task. With its automatically generated GTI file, *espfilt* calls the *evselect* task to create filtered event files. For the manual GTI-file this had to be done by the user.

After filtering the soft protons, point sources were removed next, with the *cheese* task, which runs an automatic source detection *edetect_chain*. The *cheese* task was executed using the default values for all parameters, except the minimum distance of point sources, which was lowered from 50″ to 20″.

3.3.1 Image Production

After the point source removal with *cheese*, the further data extraction diverges into image production and the extraction of spectra. Since, in the end, we are interested in the spectra of a possible super bubble, we have to first determine if a possible region exists, and where it is. To this end, we require an image of the observed area.

With soft protons and point sources removed, we now extract the spectral data together with the quiescent-particle-background (QPB), using the *mosspectra*, *mosback*, *pnspectra* and *pnback* tasks. Since we are aiming for an image of the whole field-of-view, we specify no region for this extraction, instead generating the spectra for the whole FOV. In order to better visualize the energy distribution via an RGB composite image, the spectra and background were extracted for three energy ranges, 300-1000 keV, 1000-2000 keV and 2000-8000 keV.

While the *espfilt* task removes a significant part of the soft-proton flare, some residual contamination remains, which has to be removed with the *proton* task. Before we can use *proton*,

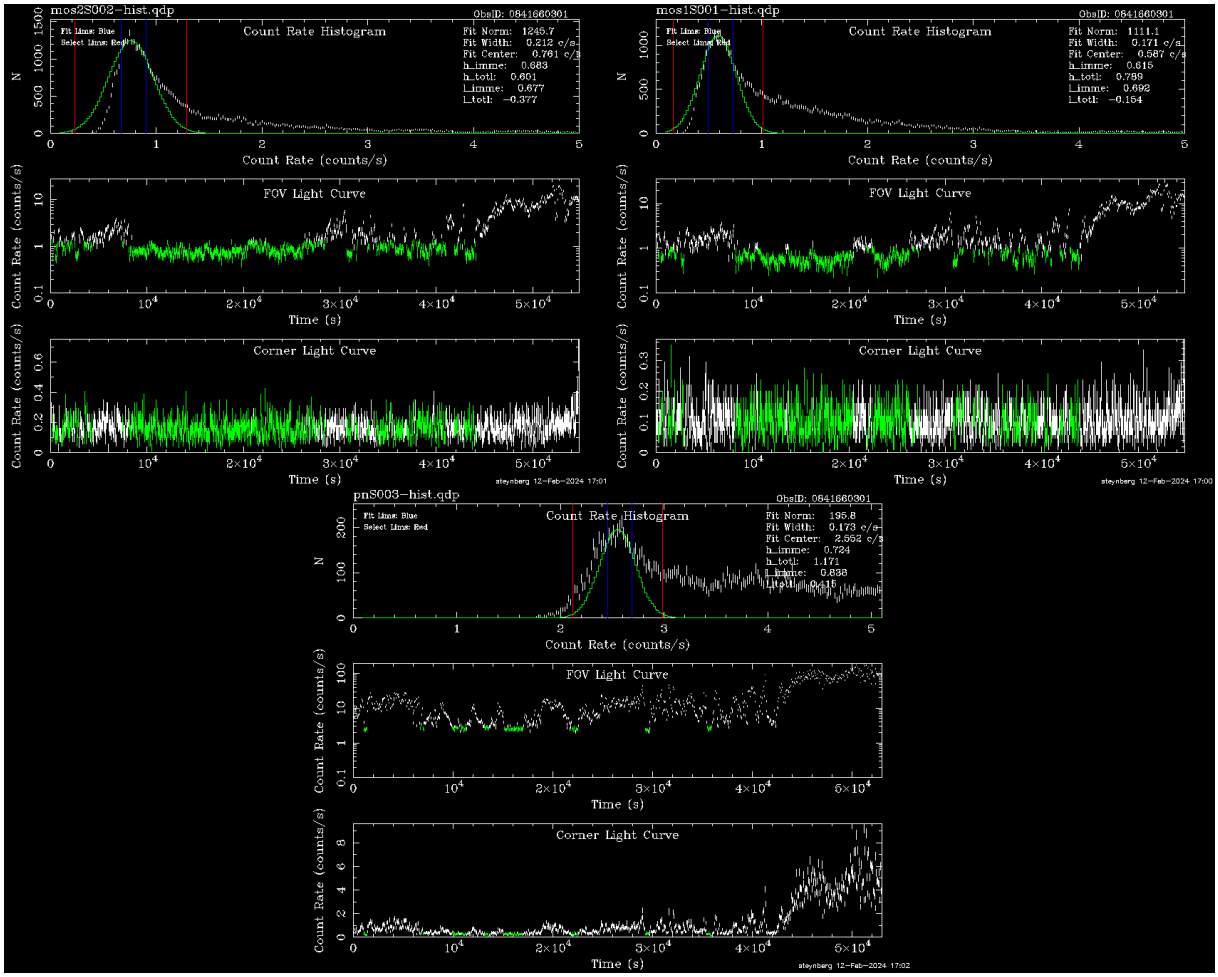

Figure 3.4: Depicted are the field-of-view and corner light curves (middle and bottom rows), together with the count rate histogram (upper rows) for each detector, MOS1, MOS2 and PN. The images were created by the *espfilt* task, where the green parts show sections accepted for the good-time-interval (GTI), while filtering out the rest. The green curve in the histograms represents the gaussian *espfilt* fits to the data, to determine the 1.5σ thresholds for accepted count rates.

we are required to model and fit the remaining soft-proton contamination for the entire FOV. The model used for the fit is the same basic model used for the spectral analysis, which is given in equation 4.1.1. For the soft proton removal, a simple, apec component is used so model the source component (*SOURCE*[4]). The actual soft proton background is simultaneously fitted for each detector as a separate model, consisting of a single powerlaw component. The *proton* task requires both, the photon index and normalization (see table 3.1) of each model, to produce an image of the SP background, which is later used to remove the remaining soft proton contamination. The photon index (PhoIndex) of MOS1 and MOS2 are tied to each other and set equal.

Table 3.1. Fit values for the parameters of the soft proton powerlaw-model.

Detector	Parameter	Value
MOS1	PhoIndex	0.9206
	Norm.	0.1180
MOS2	PhoIndex	0.9206
	Norm.	0.1113
PN	PhoIndex	9.5
	Norm.	2.245×10^{-4}

The SAS software package also offers the possibility to remove contamination by solar-wind-charge-exchange (SWCX), using the *swcx* task, which in turn would also require a fit of the entire FOV data, in order to determine the parameters of specific SWCX-lines. Since the heavily flare contaminated data offers only limited statistics, making the already demanding fit of SWCX-lines even more difficult, the removal of solar-wind-charge-exchange contamination was omitted.

The second to last step for the image production consists of running the *combimage* task, to combine and properly scale the image data of the different detectors.

In the final step the task *binadapt* is run, which creates an exposure and background corrected image, with the option of additional binning and/or smoothing. Overall, we repeat the last two steps three times, once for every energy band, that we defined during the extraction.

Figure 3.5 shows the results of the image production above. On the left, an RGB composite image of all three energy bands is shown, while the right side only depicts the soft X-ray emission, with the contour outlined in green. The field of view is dominated by a 3 arcmin wide region of soft X-rays, which encompasses a central bulge, a diffuse extension to the east and a crescent like structure to the west.

X-ray emission of intermediate energies are dispersed throughout the region, with two significant concentrations, one in the upper half of the bulge and the other in the upper part of the western structure. There appears to be no significant emission of hard X-rays.

3.3.2 Comparison with Optical Data

The X-ray images produced in the previous section clearly show a diffuse emission of soft X-rays. To verify possible structures and determine regions of interest, a comparison with optical data was performed.

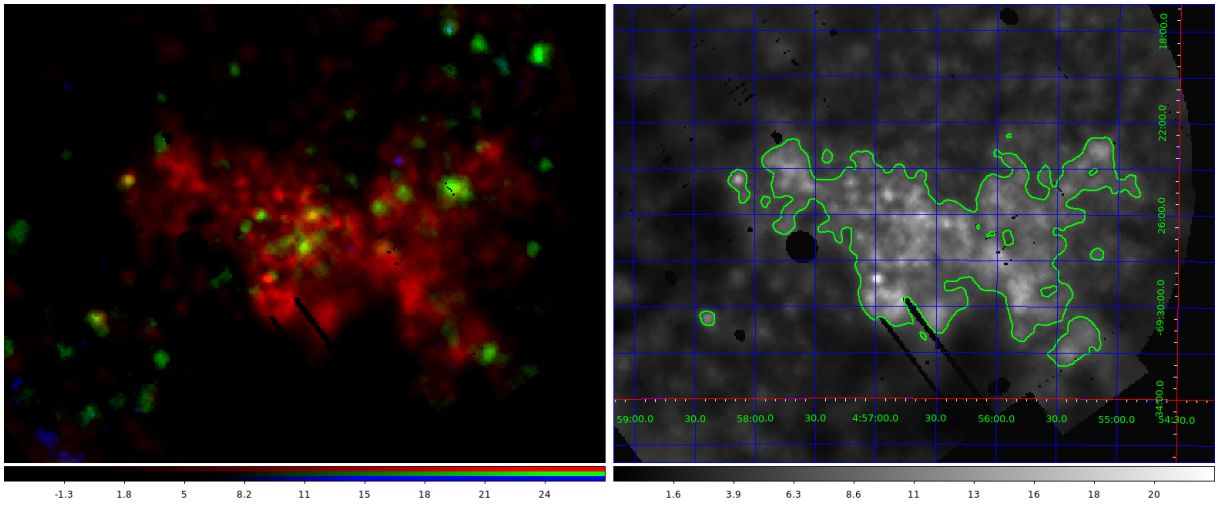

Figure 3.5: On the left hand side, an RGB-image of the extracted X-ray data is shown, with red for soft (300-1000 keV), green for intermediate (1000-2000 keV) and blue for hard (2000-8000 keV) X-ray emission. The right hand side shows a greyscale image of only the soft emission, with the contour marked in green.

For this purpose, data from the *Magellanic Emission Line Survey* (MCELS) by Smith et al., 2005, was used, specifically the Hα, [OIII] and [SII] line data. The three line emission images were combined into an RGB composite image with Hα in the red, [SII] in the green and [OIII] in the blue channel (see figure 3.6 left).

In the optical image, a semicircle-like structure is clearly visible to the south, with emission in the north that could to be part of the same shell.

In order to compare the X-ray and the optical images, the soft X-ray contour from figure 3.5 was drawn on top of the optical RGB-image (see figure 3.6 right). The Contour follows the shell in the south perfectly, continuing with the smaller optical emission structure in the north. There appear to be two outflows causing the x-ray emission structures to the east and west of the bulge.

To check for possible stellar populations, the position of massive stars in the LMC, given by Bonanos et al., 2009, is displayed in the right hand side image of figure 3.6, with Wolf-Rayet (WR) stars marked in cyan and O-type stars in magenta. The only known massive star within the diffuse X-ray emission region, is a WR star on the western side of the shell/bulge.

Based on the optical RGB-image image in figure 3.6, in conjunction with the soft X-ray contour, the shell-like structure is identified as a possible superbubble and a circular region is defined as source for spectral extraction.

Figure 3.7 shows the optical image from figure 3.6 together with the soft X-ray contour, the

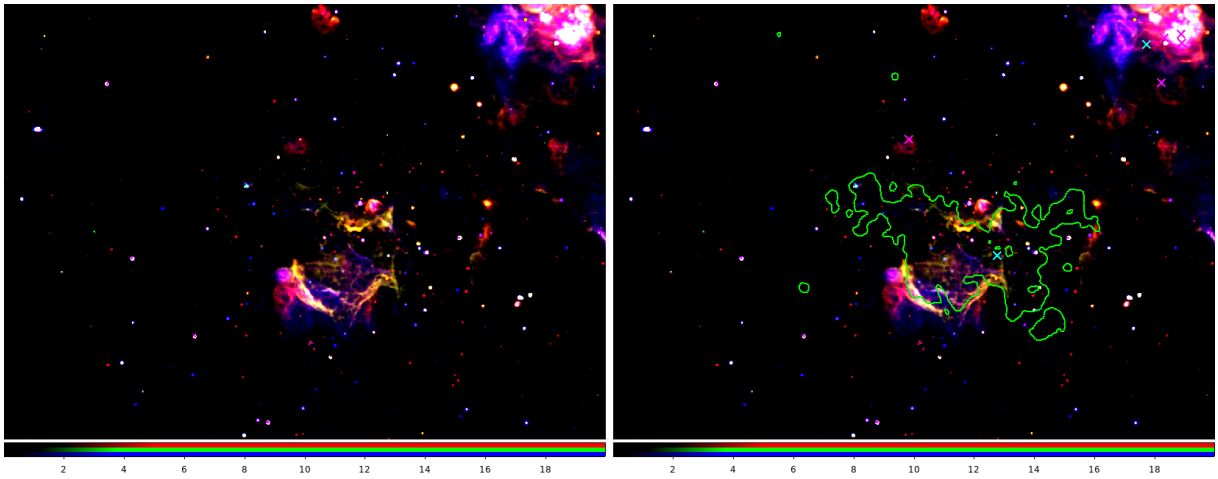

Figure 3.6: On the left hand side, an RGB-image of the MCELS Hα(red), [SII] (green) and [OIII] (blue) data. The right hand side shows the RGB-image overlaid with the soft X-ray contour from figure 3.5 (right) and known massive stars in the region given by Bonanos et al., 2009. Wolf-Rayet (WR) stars are marked in cyan, O-type stars in magenta. The only known massive star in the X-ray emission region is a WR star at the western edge of the bulge/shell.

source region (magenta) and the area chosen as background region (cyan).

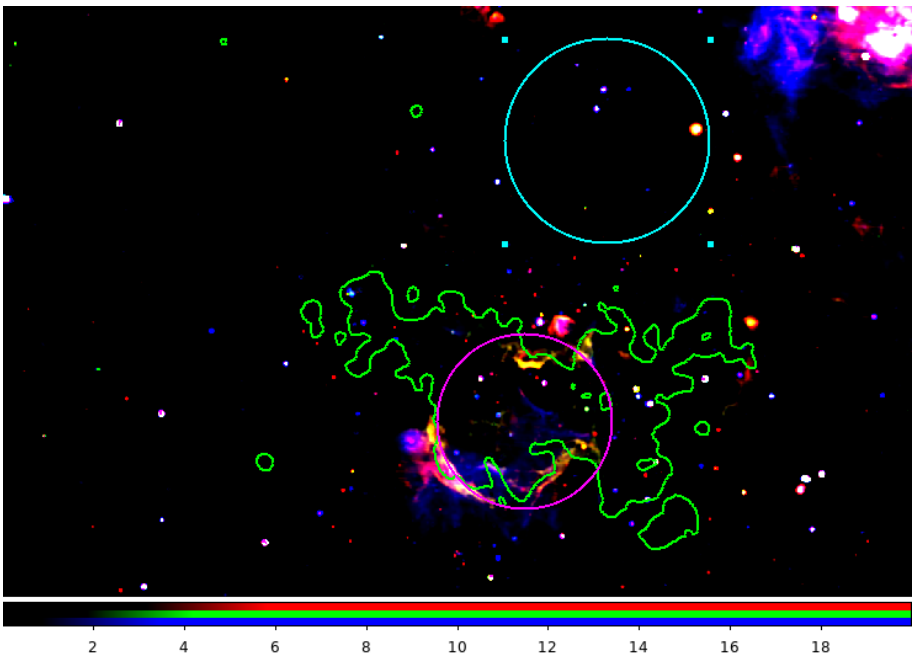

Figure 3.7: Displayed here, is the RGB-image from figure 3.6 together with the soft X-ray contour and the areas chosen as source and background regions for the spectral extraction. The circular bubble region colored in magenta is chosen as source, with the region colored in cyan chosen as background region.

CHAPTER 4

Spectral Analysis

After identifying a region of diffuse, mainly soft, X-ray radiation in the images shown in figure 3.5, and finding a corresponding shell-like structure in an optical MCELS image (see fig. 3.6), the presence of a superbubble was assumed.

In order to study the properties of this superbubble, a spectral analysis was conducted, which required the extraction of spectral data in the region of the bubble, as well as a background region.

The chosen regions are displayed in figure 3.7, with the source/bubble region drawn in magenta and the background region drawn in cyan. The spectral data was then extracted by repeating the ESAS tasks from the flowchart in figure 3.3, limited to the chosen regions and for an energy range from 0.2-10 keV.

In a last step, the source and background spectra were binned, with a minimum of 50 counts in each bin, and each were grouped with their corresponding QPB, ARF and RMF files.

4.1 Xspec Model

The spectral analysis, in form of a model parameter fit, was conducted using the *XSpec, X-Ray Spectral Fitting Package* developed by Arnaud et al., 2023. The basic model used for all fits is given in equation 4.1.1 and built from the following components:

- Gaussians covering different instrument intrinsic lines and possible solar-wind-charge-exchange (SWCX) contamination
- Two *constant* parameters, equal to the effective area in arcmin, covered by each instrument

Table 4.1. Values for the *constant* components, calculated with the *proton_scale* task for each detector and region.

Region	MOS 1	MOS 2	PN
Source	19.679	34.566	33.483
Background	32.912	38.641	40.828

- An unabsorbed component for the local hot bubble, $apec[1]$
- An absorption component for the ISM, $TBabs$
- A warm and cold component for the galactic halo, $apec[2]$ and $apec[3]$
- A component for the unresolved extra-galactic background, *powerlaw*
- One or more apec/nei components for the source emission, $SOURCE$
- An absorption component for the LMC, $TBvarabs$

$$\begin{aligned} &gaussians + constant \cdot (apec[1] + TBabs \cdot (apec[2] + apec[3] + powerlaw)) \\ &+constant \cdot TBabs \cdot TBvarabs \cdot SOURCE \end{aligned} \tag{4.1.1}$$

The values for the *constant* parameters, corresponding to the effective area of the extraction region, are calculated using the *proton_scale* task and listed in table 4.1.

X-Ray emitting components are the $apec$ component, a collisionally ionized plasma, the *nei* component, a non-equilibrium ionization plasma and the *powerlaw* component, used for non-resolved extra galactic emission and remaining soft-proton contamination. The $TBabs$ and $TBvarabs$ components by Wilms et al., 2000, model absorption through the galactic and LMC's ISM.

The model from equation 4.1.1 is implemented six times, once for each region, source and background, and within each region, once for every detector, MOS1, MOS2 and PN. Parameters that were expected to be the same across all six models, were linked.

The detectors have their own ancillary-response-file (ARF) and response-matrix-file (RMF) for each region, through which the corresponding model is folded. Since no ARF is necessary for the soft-proton emission, and a separate diagonal unitary matrix acts as RMF, the *powerlaw* components modeling the SP contamination are implemented as separate, region independent models for each detector.

4.2 Xspec fits

The energy range for the spectral fitting was limited to 0.4 keV - 5 keV, since the spectra were heavily flare contaminated for lower energies.

Since the local hot bubble predominantly emits X-Rays below 0.4 keV, the fits proved to be insensitive to the parameters of the local hot bubble component (*apec*[1]). For this reason, the normalization of *apec*[1] was set to zero, de facto removing the local hot bubble background component.

The remaining two background *apec* components for the cold and warm galactic halo were only fitted via their normalization parameter, with the temperatures set to literature values of $kT_{\text{cold}} = 0.15\,\text{keV}$ and $kT_{warm} = 0.5\,\text{keV}$, see e.g. Das et al., 2019.

The hydrogen-column values, $nH = 8.16 \times 10^{20}\,\text{cm}^{-2}$, for the *TBabs* component were taken from the HI survey by the HI4PI Collaboration et al., 2016, at the coordinates of the XMM observations pointing: RA: $74^\circ 16' 57.0''$ and DEC: $-69^\circ 23' 58.0''$.

To model the reduced LMC metal abundances, the *TBvarabs* component was integrated into the model, with all elements, except Helium, set to 50% of their corresponding galactic values. The effective area for the two constants was calculated with the *proton_scale* task.

The Gaussian components model two instrument lines at energies $E = 1.49\,\text{keV}$ and $E = 1.75\,\text{keV}$, and a 0.92 keV solar-wind-charge-exchange (SWCX) line. The normalization of the lines is initially set to zero, and only after a stable fit is found are the Gaussians fit one by one, with the SWCX line being fit last.

For the source component (*SOURCE*) three different constellations were fitted, a single *nei* component, two *nei* components and two *apec* components.

4.2.1 NEI Source Model

The first fit uses a single *nei* component as source model, assuming the source is a plasma, which is not in ionization equilibrium, with a single ionization parameter and temperature element. The spectral data from all detectors, together with the fitted model is shown in figure 4.1, with a different color for each detector and extraction region. The lower panel shows the residuals of the fit in units of sigma, with one sigma error bars. For the fit-statistic a χ^2-value of 1520.56 with 1336 degrees-of-freedom (DoF) was obtained. The Null-Hypothesis probability came to 3.01×10^{-4}.

For the single *nei*-source model, three Gaussian line components were fitted, two for the instrument lines and a single 0.92 keV line for SWCX contamination.

Table 4.2. Normalization values, in units of 10^{-5}, for the Gaussian lines in the source and background model with a single *nei* source component. The lower and upper limits of the 90% confidence interval are given.

Region	Line Energy	MOS 1	MOS 2	PN
Source	0.92 keV	-	$1.58^{2.02}_{1.12}$	$2.05^{2.42}_{1.69}$
	1.49 keV	$1.58^{1.79}_{1.37}$	$3.14^{3.42}_{2.87}$	$1.26^{1.47}_{1.05}$
	1.75 keV	$0.71^{0.89}_{0.54}$	$1.11^{1.32}_{0.91}$	-
Background	0.92 keV	$0.17^{0.51}_{0}$	-	$0.24^{0.60}_{0}$
	1.49 keV	$3.74^{4.08}_{3.41}$	$4.85^{5.23}_{4.48}$	$1.91^{2.18}_{1.65}$
	1.75 keV	$1.10^{1.36}_{0.85}$	$1.42^{1.69}_{1.16}$	-

The fit-values are listed in table 4.2 for the source and background region. It should be noted, that the PN-detector only requires one line and that the SWCX line was not always present. In these cases no fit value is given.

The fit-values for the galactic background components are listed in table 4.3, with the temperature parameters of the *apec* components and the photon-index of the *powerlaw* component frozen to common literature values, see e.g. Das et al., 2019, and Hickox and Markevitch, 2006, as the fit was unstable with these parameters set as free.

Figures 4.2, 4.3 and 4.4 show the spectra and model, together with the additive components, for the source (black) and background (red) extraction regions. In all three images, the source *nei* component is highlighted in blue. As with figure 4.1, the lower panel displays the residuals.

As the soft-proton flares could not be removed in the first steps of the extraction process, see fig. 3.3, due to the high flare amount requiring a manual determination of the good-time interval, the SP contamination is fitted separately from the extraction regions with a powerlaw model. The photon index must be the same for MOS 1 and MOS 2, so these parameters are linked during the fit. The fit values are listed in table 4.4.

The fit results for the source component are listed in table 4.5, showing a temperature of $kT = 0.23\,\text{keV}$, corresponding to $\sim 2.7 \times 10^6\,\text{K}$, indicating a hot plasma. The fit also proved to be insensitive to the ionization timescale τ, apparent by the large 90% confidence interval.

4.2.2 Two-NEI Source Model

To examine the possibility of two distinct plasmas producing the diffuse emission, a fit with two separate *nei* components, acting as source, was conducted. The fitted model, together with

Table 4.3. Parameter values from the Galactic background components for the single-*nei* model. These are identical for the source and background region, as well as for the different detectors, since the constant parameters scale the effective detector area. The lower and upper limits of the 90% confidence interval are given, except for frozen parameters.

Component	Parameter	Fit-value
apec[2]	Temp. [keV] (frozen)	0.15
	Norm.	$4.40^{4.99}_{3.87} \times 10^{-6}$
apec[3]	Temp. [keV] (frozen)	0.50
	Norm.	$4.96^{6.05}_{3.75} \times 10^{-7}$
powerlaw	PhoIndex (frozen)	1.46
	Norm.	$2.36^{2.72}_{2.02} \times 10^{-6}$

Table 4.4. Parameter values for the soft-proton background from the single-*nei* model fit. The values for the source, as well as the background region are shown. The lower and upper limits of the 90% confidence interval are given.

Detector	Parameter	Source	Background
MOS 1	PhoIndex	$0.71^{0.79}_{0.62}$	$0.55^{0.63}_{0.46}$
	Norm. [10^{-2}]	$1.92^{2.13}_{1.72}$	$2.20^{2.44}_{1.96}$
MOS 2	PhoIndex	=MOS 1	=MOS 1
	Norm. [10^{-2}]	$1.53^{1.81}_{1.29}$	$1.18^{1.39}_{0.97}$
PN	PhoIndex	$0.53^{0.61}_{0.45}$	$0.40^{0.48}_{0.31}$
	Norm.	$0.11^{0.12}_{0.09}$	$8.79^{9.77}_{7.85} \times 10^{-2}$

Table 4.5. Parameter values from the source *nei* component. The lower and upper limits of the 90% confidence interval are given.

Component	Parameter	Fit-value
nei	Temp. [keV]	$0.23^{0.26}_{0.22}$
	τ [s/cm^3]	$8.61^{14.3}_{3.88} \times 10^{11}$
	Norm.	$1.52^{1.72}_{1.14} \times 10^{-5}$

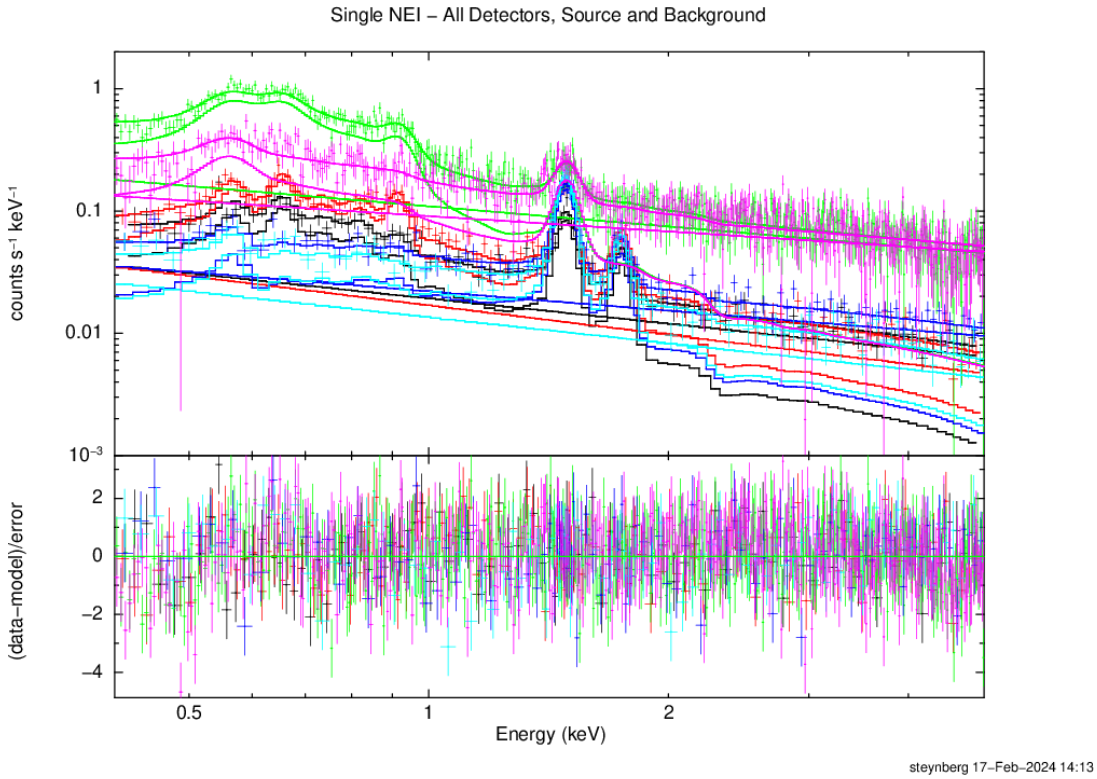

Figure 4.1: In this image, the spectral data for all detectors, as well as the fitted model with a single *nei* source component is shown. The colors correspond to the detectors and extraction region in the following order:
MOS 1 - Source (black); MOS 2 - Source (red); PN - Source (green); MOS 1 - Background (blue); MOS 2 - Background (cyan); PN - Background (magenta)
The lower panel shows the residuals in units of sigma, with error bars of one sigma.

the spectral data is displayed in figure 4.5 for all detectors, from both source and background, extraction regions. The lower panel again shows the residuals of the fit. For this two-*nei* source component fit, the χ^2-value came to 1287.03 with 1161 DoF and a Null-hypothesis probability of 5.54×10^{-3}.

The two-*nei* model fits the same Gaussian lines as the single-*nei* model, with the fit results for the normalizations listed in table 4.6. The values for the galactic background components, which were fitted via the same parameters as with the single-*nei* model, are listed in table 4.7. Lastly the results for the SP-background can be found in table 4.8.

A separate plot of the spectral data and fitted model, for each detector, is shown in figures 4.6, 4.7 and 4.8, with the source region data plotted in black and the background region in red.

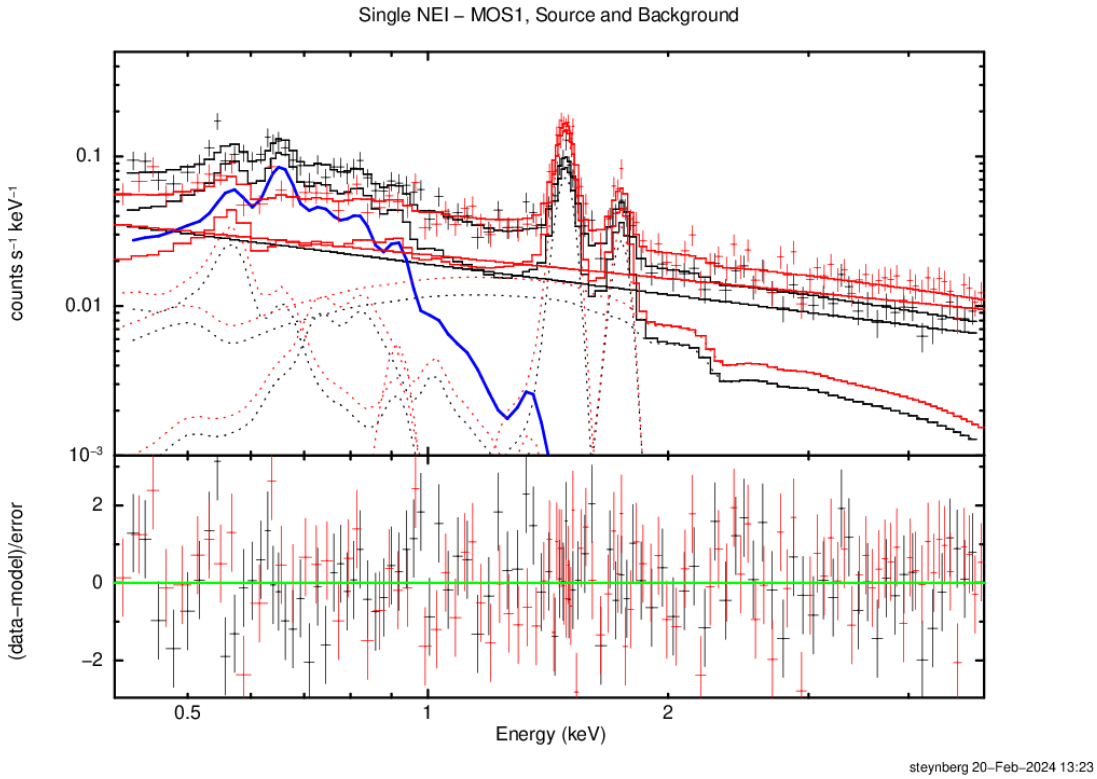

Figure 4.2: In this image, the spectral data for the MOS 1 detector, as well as the fitted model with a single *nei* source component, including the additive components is shown. The source spectrum is shown in black, with the background in red. The source *nei* component is highlighted in blue. The lower panel shows the residuals in units of sigma, with error bars of one sigma.

The additive components are also shown as dashed lines, with the two source *nei* components highlighted in blue and purple.

The parameter values of the source *nei* components are listed in table 4.9, showing a colder ($kT = 0.23\,\mathrm{keV}$) and a warmer ($kT = 3.65\,\mathrm{keV}$) temperature for each component. The cold and warm temperature values correspond to $T_{\mathrm{cold}} \sim 2.7 \times 10^6\,\mathrm{K}$ and $T_{\mathrm{warm}} \sim 4.2 \times 10^7\,\mathrm{K}$ respectively. The fit was again insensitive to the ionization timescale parameter τ, even requiring the τ-value for *nei*[2] to be frozen.

Table 4.6. Normalization values, in units of 10^{-5}, for the Gaussian lines in the source and background model with two *nei* source components. The lower and upper limits of the 90% confidence interval are given.

Region	Line Energy	MOS 1	MOS 2	PN
Source	0.92 keV	$0.16^{0.47}_{0}$	$1.50^{1.93}_{1.08}$	$2.14^{2.5}_{1.81}$
	1.49 keV	$1.52^{1.74}_{1.30}$	$3.00^{3.28}_{2.71}$	$1.23^{1.45}_{1.00}$
	1.75 keV	$0.69^{0.87}_{0.51}$	$1.05^{1.27}_{0.83}$	-
Background	0.92 keV	$0.21^{0.55}_{0.00}$	-	$0.36^{0.72}_{0.00}$
	1.49 keV	$3.89^{4.23}_{3.55}$	$5.00^{5.34}_{4.62}$	$1.97^{2.25}_{1.70}$
	1.75 keV	$1.20^{1.46}_{0.95}$	$1.51^{1.78}_{1.24}$	-

Table 4.7. Parameter values from the Galactic background components for the two-*nei* model. These are identical for the source and background region, as well as for the different detectors, since the constant parameters scale the effective detector area. The lower and upper limits of the 90% confidence interval are given, except for frozen parameters.

Component	Parameter	Fit-value
apec[2]	Temp. [keV] (frozen)	0.15
	Norm.	$4.18^{4.77}_{3.58} \times 10^{-6}$
apec[3]	Temp. [keV] (frozen)	0.50
	Norm.	$5.44^{6.60}_{4.33} \times 10^{-7}$
powerlaw	PhoIndex (frozen)	1.46
	Norm.	$1.50^{1.93}_{1.06} \times 10^{-6}$

Table 4.8. Parameter values for the soft-proton background from the two-*nei* model fit. The values for the source, as well as the background region are shown. The lower and upper limits of the 90% confidence interval are given.

Detector	Parameter	Source	Background
MOS 1	PhoIndex	$0.48^{0.61}_{0.32}$	$0.61^{0.68}_{0.53}$
	Norm. [10^{-2}]	$1.44^{1.70}_{1.13}$	$2.57^{2.83}_{2.30}$
MOS 2	PhoIndex	=MOS 1	=MOS 1
	Norm. [10^{-2}]	$0.99^{1.33}_{0.63}$	$1.61^{1.87}_{1.35}$
PN	PhoIndex	$0.22^{0.34}_{0.06}$	$0.40^{0.49}_{0.30}$
	Norm.	$7.73^{9.16}_{6.24} \times 10^{-2}$	$0.10^{0.12}_{0.09}$

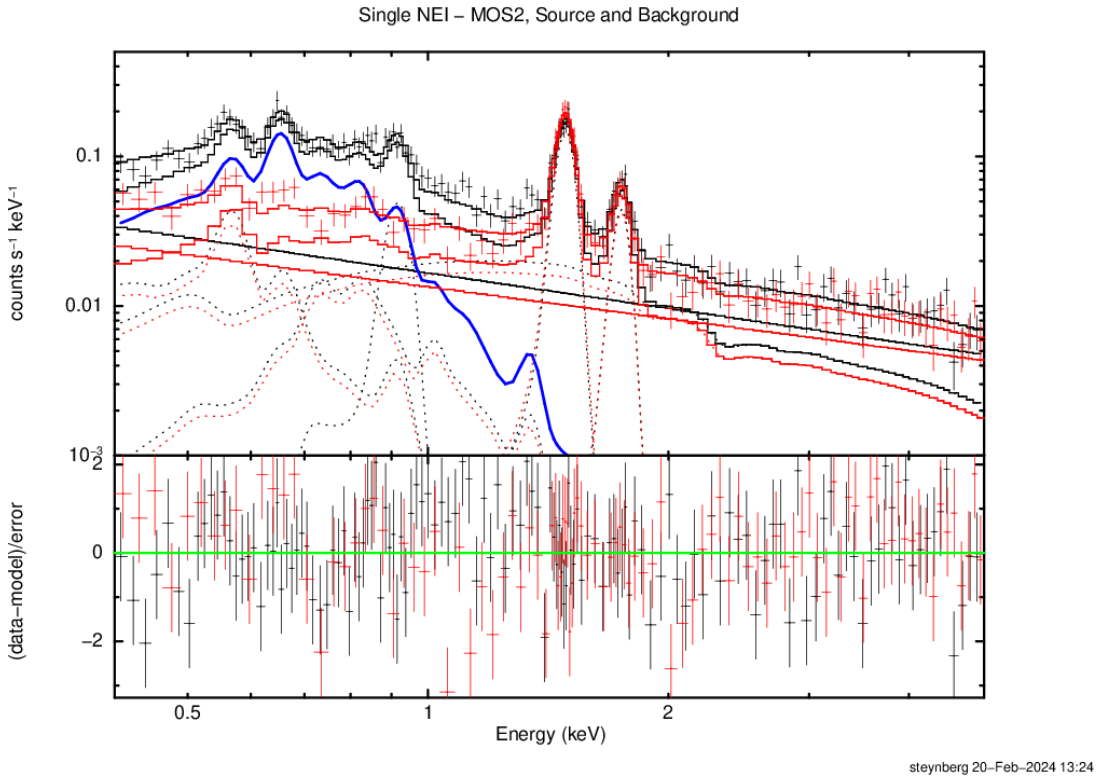

Figure 4.3: In this image, the spectral data for the MOS 2 detector, as well as the fitted model with a single *nei* source component, including the additive components is shown. The source spectrum is shown in black, with the background in red. The source *nei* component is highlighted in blue. The lower panel shows the residuals in units of sigma, with error bars of one sigma.

4.2.3 Two-APEC Source Model

Since the fits with the *nei* source components were insensitive to the ionization timescale τ, a third model with two *apec* source components was tested. With this, a collisionally ionized plasma with two temperature components is assumed. A plot of the data, from all detectors, as well as both source and background region, is shown in figure 4.9 together with the fitted model.

As with all previous spectral plots, the lower panel displays the residuals in units of sigma, with error bars of one sigma. For this model, with two *apec* source components, the fit has a χ^2-value of 1541.70 with 1339 DoF and a Null-hypothesis probability of 8.92×10^{-5}.

With the two-*apec* source model, only two Gaussian lines, the instrument lines at 1.49 keV and 1.75 keV, were fitted. The resulting fit values for their normalizations are listed in table 4.10.

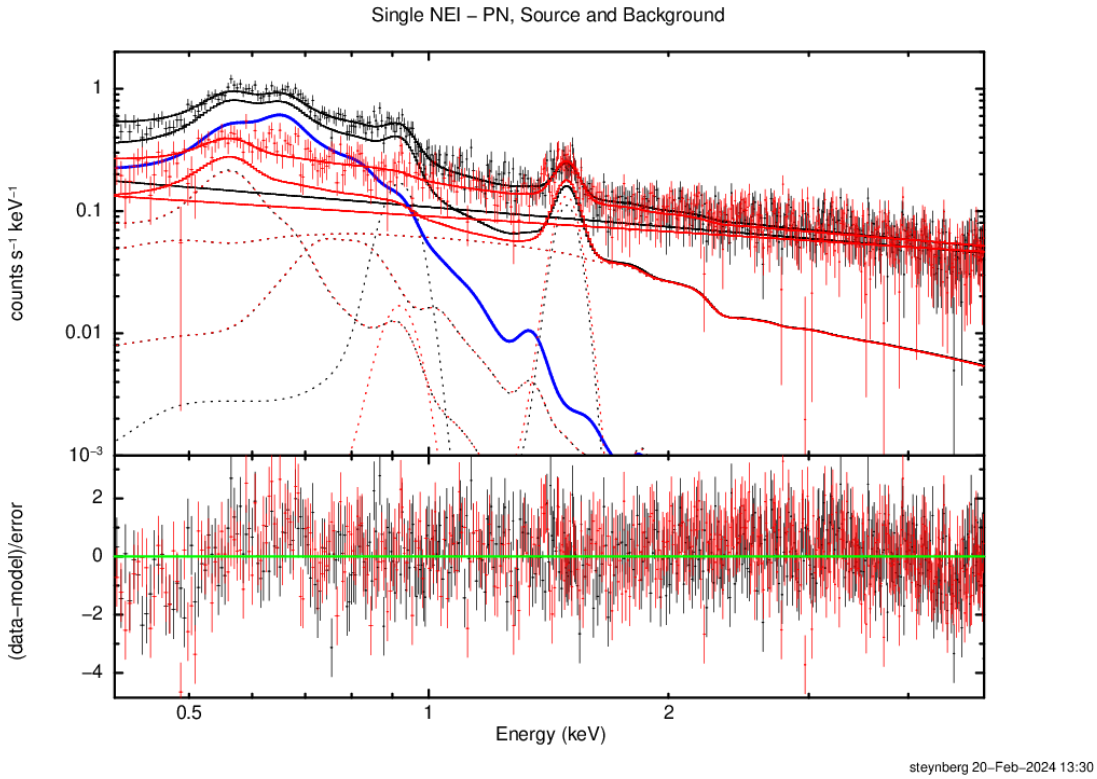

Figure 4.4: In this image, the spectral data for the PN detector, as well as the fitted model with a single *nei* source component, including the additive components is shown. The source spectrum is shown in black, with the background in red. The source *nei* component is highlighted in blue. The lower panel shows the residuals in units of sigma, with error bars of one sigma.

As with the previous *nei* source models, the galactic background components were solely fitted via their normalizations, with their temperatures set to common values.

The fit results are given in table 4.11. The final background component, the soft-proton contamination, is fitted, as with the previous cases, with a separate *powerlaw* component for each detector. The results can be found in table 4.12, with the photon index for MOS 1 and MOS 2 linked.

Figures 4.10, 4.11 and 4.12 show the spectral data from the source (black) and background (red) extraction region, together with the fitted model, for each detector separately. The additive components of the model are displayed as dashed lines, with the two source *apec* components highlighted in blue and purple.

Table 4.13 lists the fit values for the two *apec* source components, *apec*[4] and *apec*[5]. As

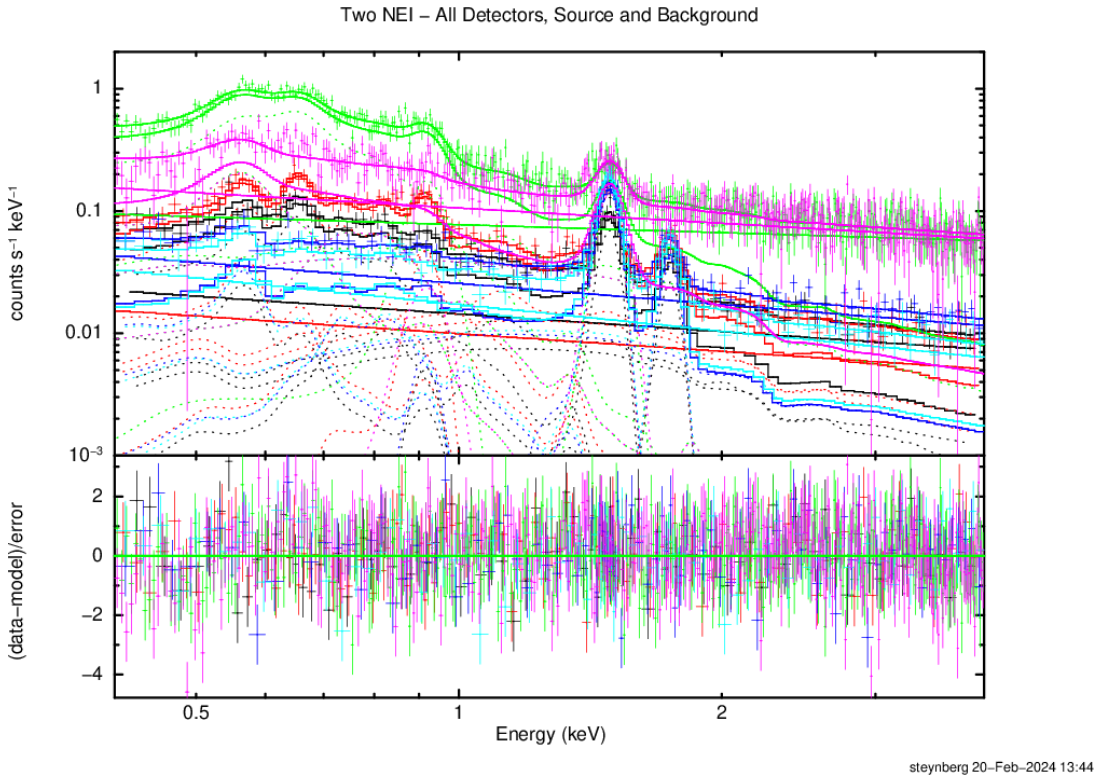

Figure 4.5: In this image, the spectral data for all detectors, as well as the fitted model with two *nei* source components is shown. The colors correspond to the detectors and extraction region in the following order:
MOS 1 - Source (black); MOS 2 - Source (red); PN - Source (green); MOS 1 - Background (blue); MOS 2 - Background (cyan); PN - Background (magenta)
The lower panel shows the residuals in units of sigma, with error bars of one sigma.

with the two *nei* components, we get two separate temperature components, a colder component *apec*[4], similar in value to *nei*[1] in table 4.9, and warmer a component *apec*[5], significantly cooler than *nei*[2]. The fit values for the temperature, $kT = 0.21\,\text{keV}$ and $kT = 0.87\,\text{keV}$, correspond to temperatures of $T_{\text{cold}} \sim 2.4 \times 10^6\,\text{K}$ and $T_{\text{warm}} \sim 1 \times 10^7\,\text{K}$.

Table 4.9. Parameter values from the two source *nei* components. The lower and upper limits of the 90% confidence interval are given.

Component	Parameter	Fit-value
nei[1]	kT [keV] (Tau frozen)	$0.23^{0.24}_{0.22}$
	τ [s/cm^3]	$8.58^{24.2}_{3.80} \times 10^{11}$
	Norm.	$1.68^{2.02}_{1.34} \times 10^{-5}$
nei[2]	kT [keV]	$3.65^{8.05}_{2.05}$
	τ [s/cm^3] (frozen)	2.55×10^{13}
	Norm.	$6.39^{9.47}_{3.65} \times 10^{-6}$

Table 4.10. Normalization values, in units of 10^{-5}, for the Gaussian lines in the source and background model with two *apec* source components. The lower and upper limits of the 90% confidence interval are given.

Region	Line Energy	MOS 1	MOS 2	PN
Source	1.49 keV	$1.61^{1.83}_{1.40}$	$3.15^{3.43}_{2.87}$	$1.30^{1.51}_{1.08}$
	1.75 keV	$0.77^{0.95}_{0.59}$	$1.16^{1.37}_{0.95}$	-
Background	1.49 keV	$3.78^{4.12}_{3.43}$	$4.91^{5.29}_{4.53}$	$1.89^{2.17}_{1.61}$
	$1.12^{1.38}_{0.87}$	$1.45^{1}_{1.18}.72$	-	

Table 4.11. Parameter values from the Galactic background components for the two-*apec* model. These are identical for the source and background region, as well as for the different detectors, since the constant parameters scale the effective detector area. The lower and upper limits of the 90% confidence interval are given, except for frozen parameters.

Component	Parameter	Fit-value
apec[2]	Temp. [keV] (frozen)	0.15
	Norm.	$3.94^{4.49}_{3.37} \times 10^{-6}$
apec[3]	Temp. [keV] (frozen)	0.50
	Norm.	$4.46^{5.54}_{3.35} \times 10^{-7}$
powerlaw	PhoIndex (frozen)	1.46
	Norm.	$1.97^{2.29}_{1.64} \times 10^{-6}$

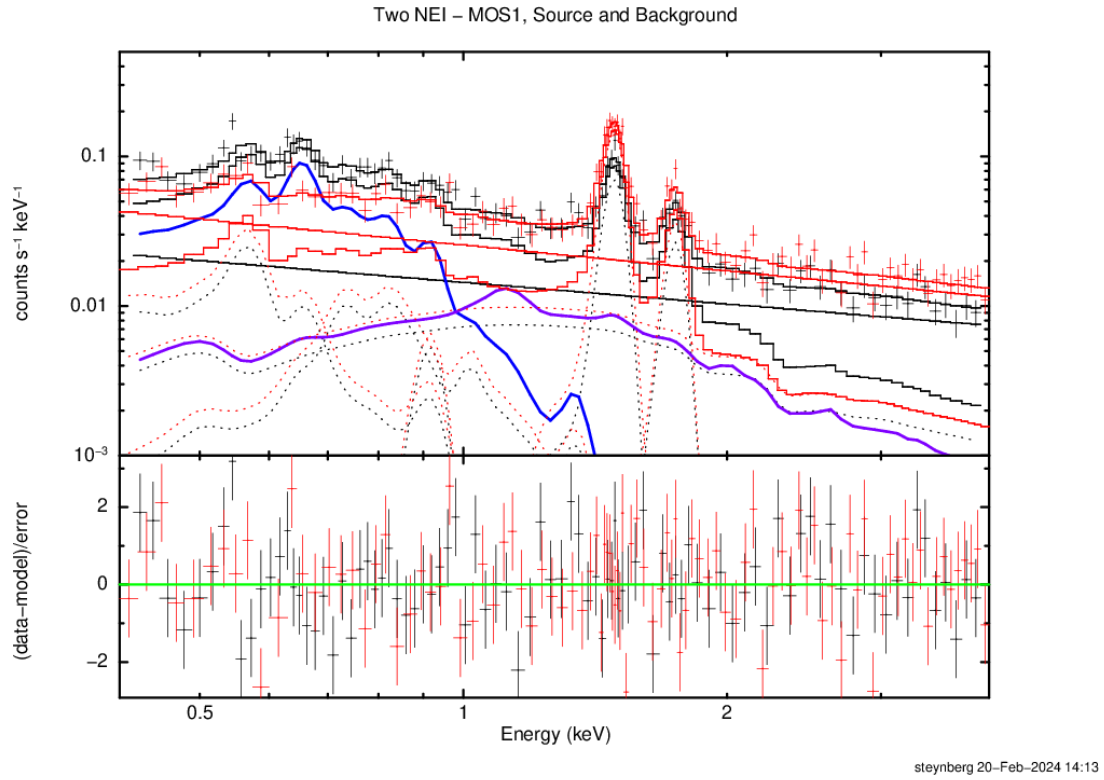

Figure 4.6: In this image, the spectral data for the MOS 1 detector, as well as the fitted model with two *nei* source components, including the additive components is shown. The source spectrum is shown in black, with the background in red. The source *nei* components are highlighted in blue and purple. The lower panel shows the residuals in units of sigma, with error bars of one sigma.

Table 4.12. Parameter values for the soft-proton background from the two-*apec* model fit. The values for the source, as well as the background region are shown. The lower and upper limits of the 90% confidence interval are given.

Detector	Parameter	Source	Background
MOS 1	PhoIndex	$0.55^{0.64}_{0.44}$	$0.61^{0.68}_{0.54}$
	Norm. $[10^{-2}]$	$1.64^{1.84}_{1.43}$	$2.48^{2.71}_{2.25}$
MOS 2	PhoIndex	=MOS 1	=MOS 1
	Norm. $[10^{-2}]$	$1.34^{1.59}_{1.10}$	$1.43^{1.64}_{1.21}$
PN	PhoIndex	$0.46^{0.53}_{0.38}$	$0.48^{0.55}_{0.40}$
	Norm.	$9.94^{10.9}_{8.96} \times 10^{-2}$	$0.10^{0.11}_{0.09}$

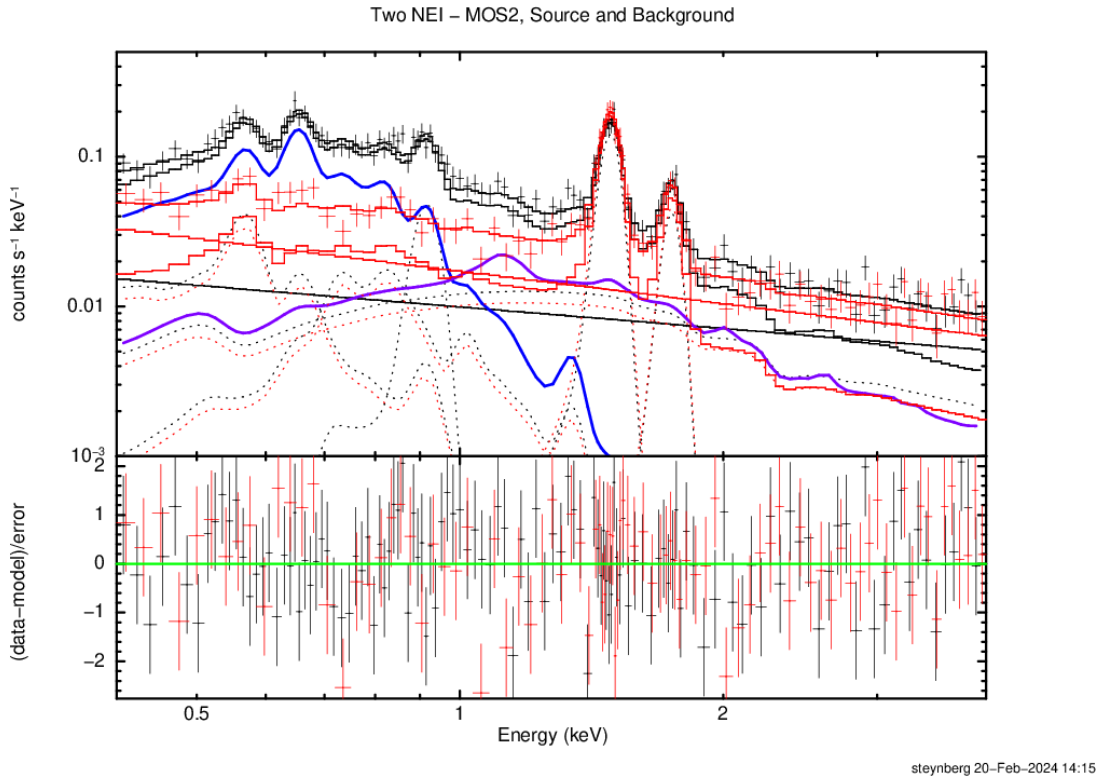

Figure 4.7: In this image, the spectral data for the MOS 2 detector, as well as the fitted model with two *nei* source components, including the additive components is shown. The source spectrum is shown in black, with the background in red. The source *nei* components are highlighted in blue and purple. The lower panel shows the residuals in units of sigma, with error bars of one sigma.

Table 4.13. Parameter values from the two source *apec* components. The lower and upper limits of the 90% confidence interval are given.

Component	Parameter	Fit-value
apec[4]	kT [keV]	$0.21^{0.22}_{0.20}$
	Norm.	$1.90^{2.01}_{1.78} \times 10^{-5}$
apec[5]	kT [keV]	$0.87^{0.94}_{0.82}$
	Norm.	$2.00^{2.33}_{1.69} \times 10^{-6}$

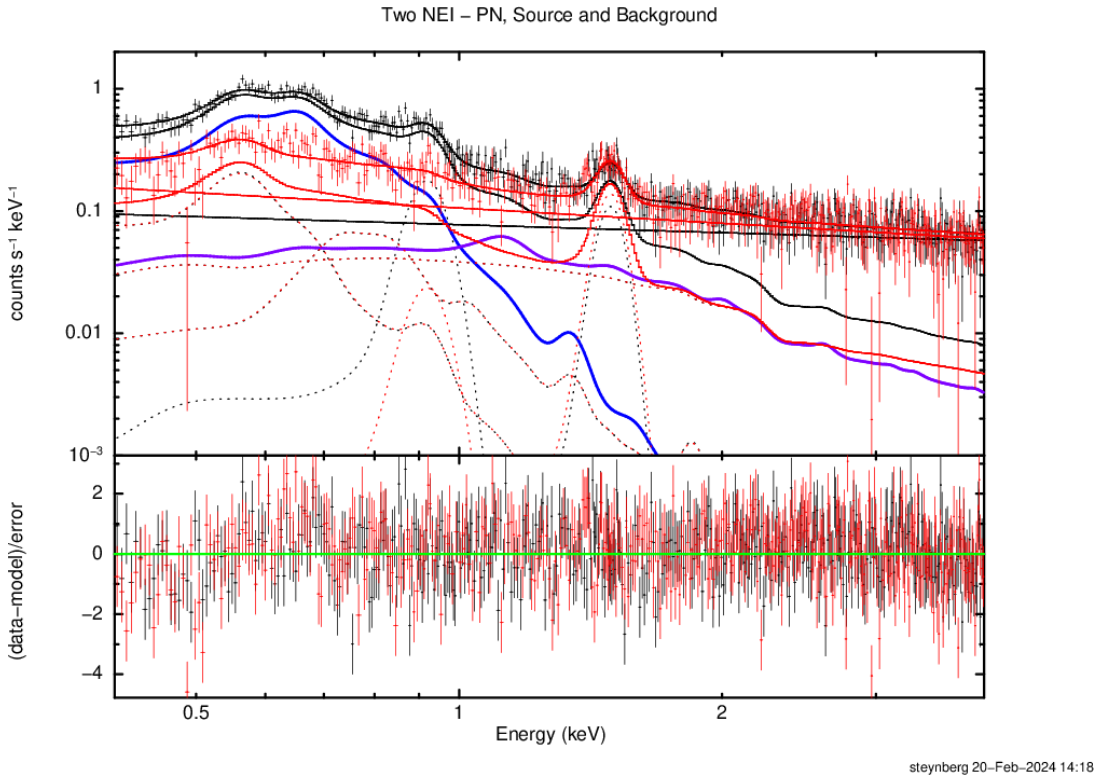

Figure 4.8: In this image, the spectral data for the PN detector, as well as the fitted model with two *nei* source components, including the additive components is shown. The source spectrum is shown in black, with the background in red. The source *nei* components are highlighted in blue and purple. The lower panel shows the residuals in units of sigma, with error bars of one sigma.

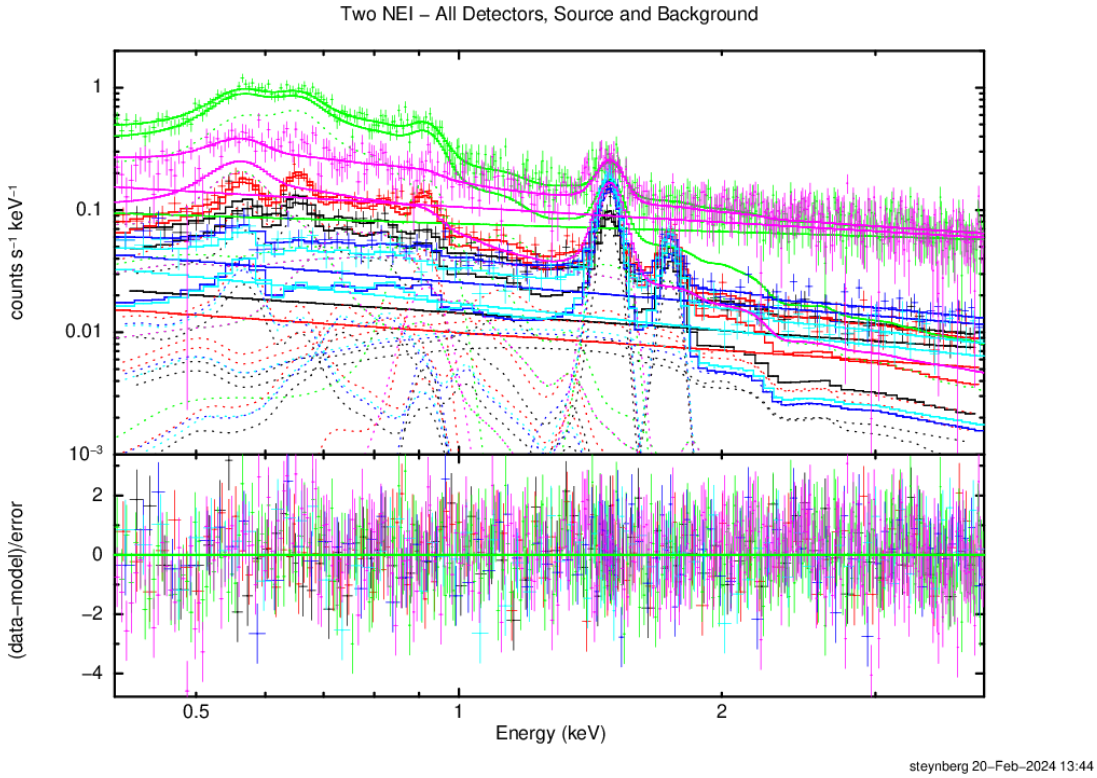

Figure 4.9: In this image, the spectral data for all detectors, as well as the fitted model with two *apec* source components is shown. The colors correspond to the detectors and extraction region in the following order:
MOS 1 - Source (black); MOS 2 - Source (red); PN - Source (green); MOS 1 - Background (blue); MOS 2 - Background (cyan); PN - Background (magenta)
The lower panel shows the residuals in units of sigma, with error bars of one sigma.

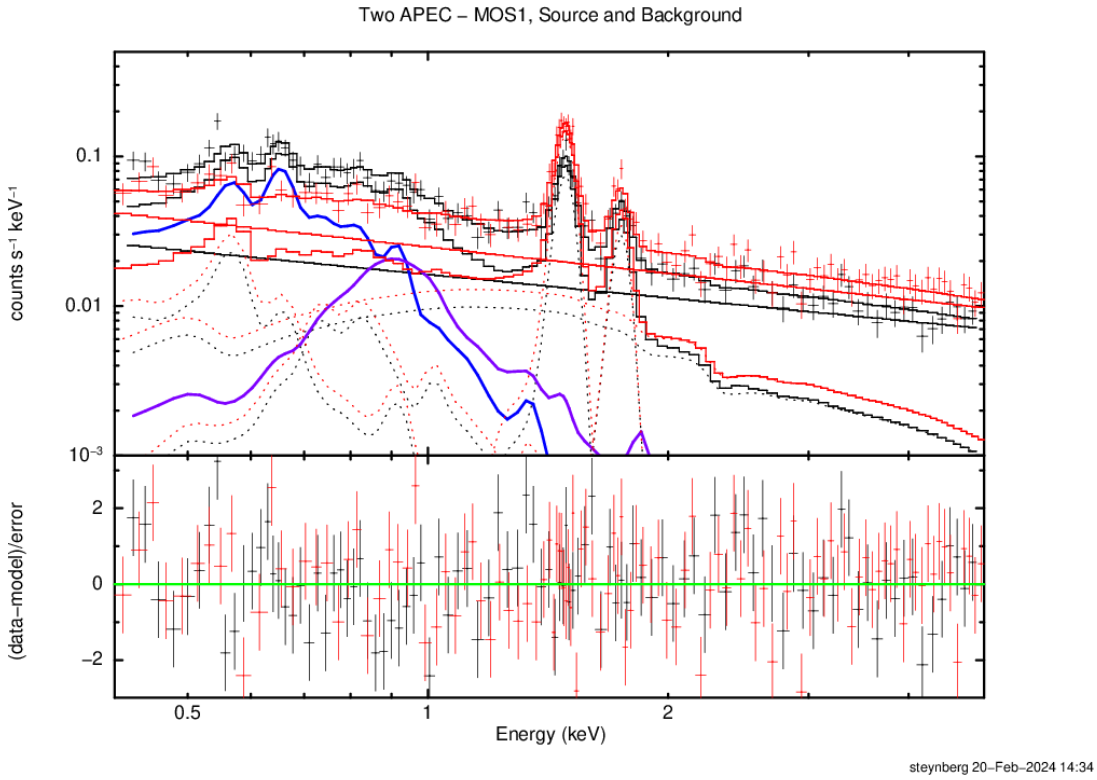

Figure 4.10: In this image, the spectral data for the MOS 1 detector, as well as the fitted model with two *apec* source components, including the additive components is shown. The source spectrum is shown in black, with the background in red. The source *apec* components are highlighted in blue and purple. The lower panel shows the residuals in units of sigma, with error bars of one sigma.

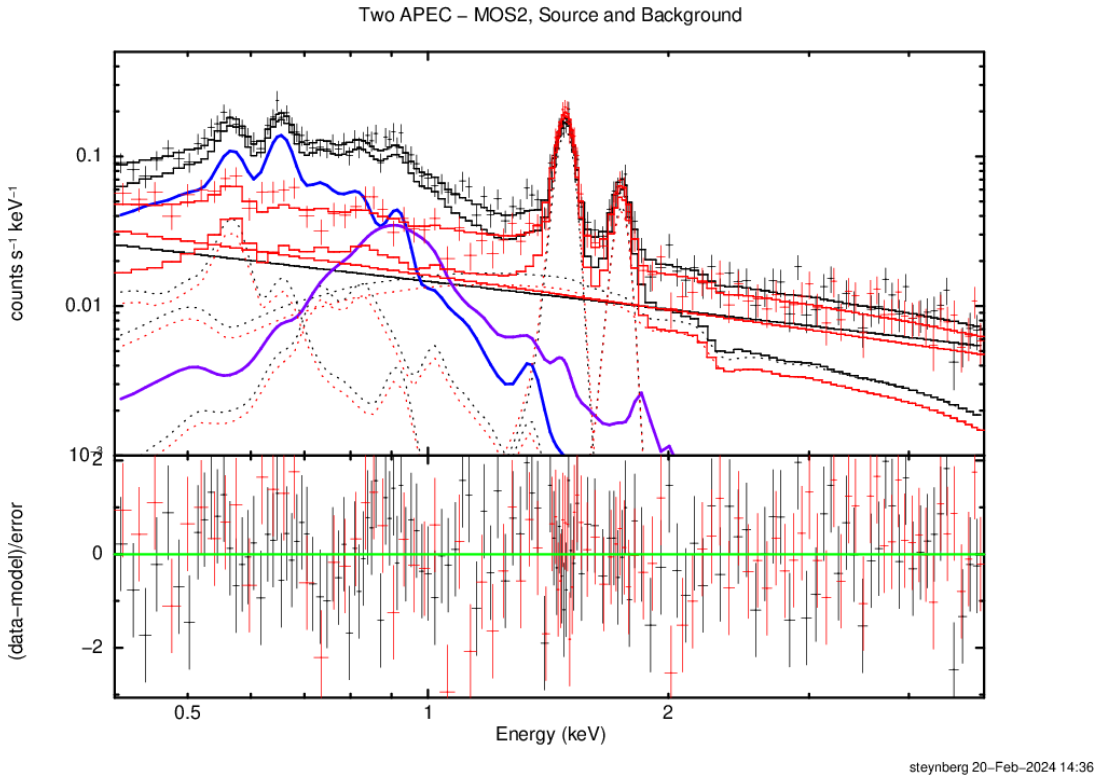

Figure 4.11: In this image, the spectral data for the MOS 2 detector, as well as the fitted model with two *apec* source components, including the additive components is shown. The source spectrum is shown in black, with the background in red. The source *apec* components are highlighted in blue and purple. The lower panel shows the residuals in units of sigma, with error bars of one sigma.

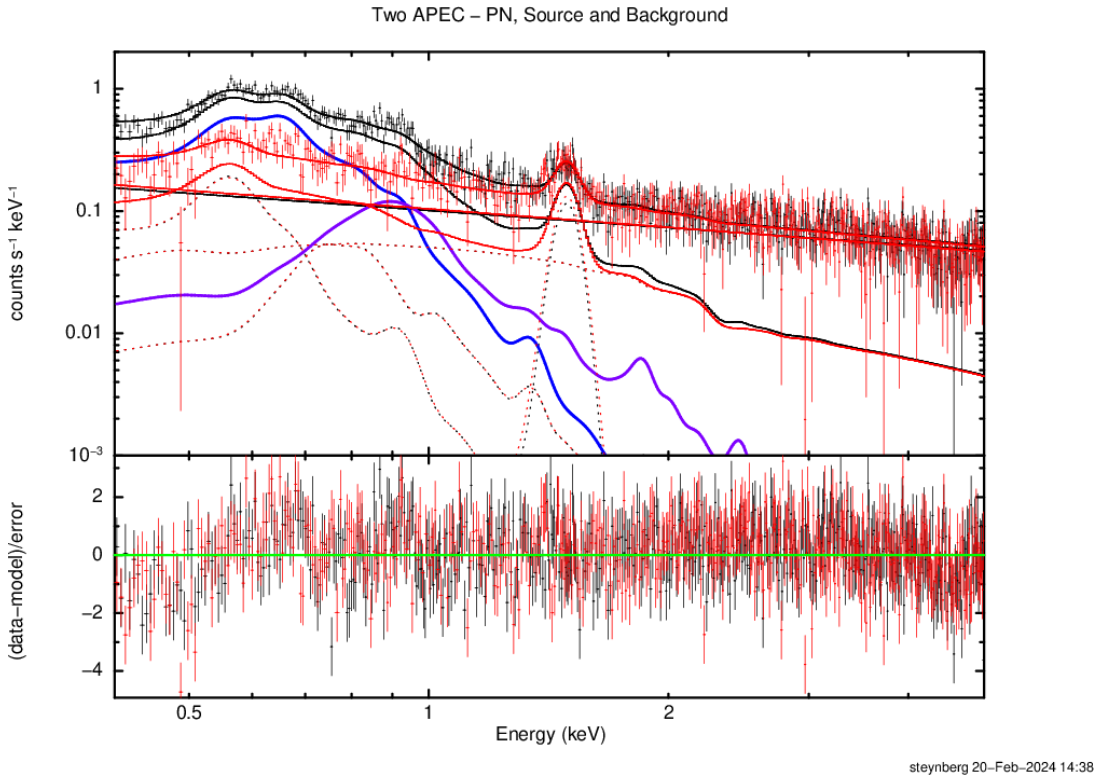

Figure 4.12: In this image, the spectral data for the PN detector, as well as the fitted model with two *apec* source components, including the additive components is shown. The source spectrum is shown in black, with the background in red. The source *apec* components are highlighted in blue and purple. The lower panel shows the residuals in units of sigma, with error bars of one sigma.

CHAPTER 5

Discussion

In this chapter, the results from the spectral analysis will be discussed. For this purpose, general properties, i.e. density, pressure and energy content of the gas within the bubble region, for the different source models, will be calculated. With these, a comparison to the energy output of massive stars, i.e. Wolf-Rayet stars and O/B-stars, will be made. To conclude the discussion, the imaging results from the Data Extraction chapter are compared to the optical counterparts, in particular a [SII]-to-Hα-ratio map.

5.1 Bubble Region Properties

First, the density of the plasma is calculated based on the normalization of the respective source parameters (*nei* or *apec*). For both components, the normalization is given by

$$norm = \frac{1}{10^{14} \times 4\pi D_{LMC}^2} \int n_e n \mathrm{d}fV, \tag{5.1.1}$$

see Arnaud et al., 2023.

The bubble region was assumed to be of approximately spherical shape, with a radius of $r = 206.29^{248.19}_{155.83}$ arcsec $\widehat{=}$ $48.00^{57.76}_{36.26}$ pc, for an LMC distance of $D_{LMC} = 48$ kpc. With this, a volume for the bubble $V = 1.36^{2.19}_{0.36} \times 10^{61}$ cm^3 is calculated. Following Sasaki et al., 2011, we calculate $n_e = (1.2+0.013\zeta_{\mathrm{LMC}})\, n \approx 1.21\, n$ with the LMC metallicity $\zeta_{\mathrm{LMC}} = 0.5$ and the hydrogen density n. We can now simplify the normalization to

$$\begin{aligned} norm &\approx \frac{1}{10^{14} \times 4\pi D_{LMC}^2} 1.21 n^2 fV \\ &= 4.39 \times 10^{-62} n^2 fV \ [\mathrm{cm}^{-5}], \end{aligned} \tag{5.1.2}$$

Table 5.1. Hydrogen density values for the different source models. The lower and upper limits of the 90% confidence interval are given.

Source Model	Normalization	Hydrogen Density [cm^{-3}]
nei	$1.52^{1.72}_{1.14} \times 10^{-5}$	$5.04^{6.61}_{3.08} \times 10^{-3}$
nei[1]+*nei*[2]	$1.68^{2.02}_{1.34} \times 10^{-5}$	$5.30^{7.00}_{3.28} \times 10^{-3}$
	$6.39^{9.47}_{3.65} \times 10^{-6}$	$3.27^{4.54}_{1.87} \times 10^{-3}$
apec[4]+*apec*[5]	$1.90^{2.01}_{1.78} \times 10^{-5}$	$5.63^{7.36}_{3.55} \times 10^{-3}$
	$2.00^{2.33}_{1.69} \times 10^{-6}$	$1.83^{2.41}_{1.14} \times 10^{-3}$

Table 5.2. Pressure values for the different source models. The lower and upper limits of the 90% confidence interval are given.

Source Model	Temperature [keV]	Pressure [cm^{-3} K]
nei	$0.23^{0.26}_{0.22}$	$3.11^{4.16}_{1.89} \times 10^4$
nei[1]+*nei*[2]	$0.23^{0.24}_{0.22}$	$3.27^{4.33}_{2.01} \times 10^4$
	$3.65^{8.05}_{2.05}$	$3.20^{7.25}_{1.24} \times 10^5$
apec[4]+*apec*[5]	$0.21^{0.22}_{0.20}$	$3.17^{4.16}_{1.99} \times 10^4$
	$0.87^{0.94}_{0.82}$	$4.26^{5.66}_{2.64} \times 10^4$

with the filling factor f.

Solving equation 5.1.2 for n gives us an equation for the hydrogen density,

$$n = 4.77 \times 10^{30} \times \sqrt{\frac{norm}{fV}} [\mathrm{cm}^{-3}]. \tag{5.1.3}$$

Table 5.1 lists the hydrogen density values for the different source components assuming a filling factor $f = 1$. With the values all lying in the range of $\sim 10^{-3}$ cm^{-3}, we can already recognize the plasma to be very thin compared to the average ISM value of 1 cm^{-3}.

With the calculated hydrogen density n and the fitted plasma temperature T, the gas pressure is given by

$$P/k = (n_e + 1.1n)T\sqrt{f} = 2.31nT\sqrt{f}, \tag{5.1.4}$$

see Sasaki et al., 2011. The pressure for the different source models is given in table 5.2, with the values being at the higher end of the galactic ISM, which is thought to have $P/k = 10^{3-4}$ cm^{-3} K.

With the pressure, we can now determine the thermal energy content within the bubble, which is given by

Table 5.3. Energy E_b values for the different source components. The last column shows the sum of the energies, in the case of multiple components. The lower and upper limits of the 90% confidence interval are given.

Source Component	Energy E_b [ergs]	Sum [ergs]	Age [Myr]	L_{SB} [erg s^{-1}]
nei	$8.76^{14.9}_{1.48} \times 10^{49}$	$8.76^{14.9}_{1.48} \times 10^{49}$	~ 2.3	1.2×10^{36}
nei[1]+*nei*[2]	$9.21^{15.6}_{1.58} \times 10^{49}$ $9.02^{21.7}_{0.41} \times 10^{50}$	$9.94^{22.7}_{1.29} \times 10^{50}$	~ 0.7	4.6×10^{37}
apec[4]+*apec*[5]	$8.94^{15.1}_{1.60} \times 10^{49}$ $1.20^{2.03}_{0.21} \times 10^{50}$	$2.10^{3.13}_{0.86} \times 10^{50}$	~ 1.5	4.5×10^{36}

$$E = 3/2 \cdot P \cdot f \cdot V, \tag{5.1.5}$$

see Sasaki et al., 2011. Table 5.3 lists the calculated values for the thermal energy content E_b of each source component, together with the sum, in the case of multiple components.

Given the energy content and radius of the bubble, we can estimate the age of the bubble with the solution for a wind blown bubble from Weaver et al., 1977, eq. 21,

$$R = \left(\frac{250}{308\pi}\right)^{1/5} L_w^{1/5} \rho_0^{-1/5} t^{3/5}, \tag{5.1.6}$$

assuming a surrounding ISM density $n_0 = 1\,\mathrm{cm}^{-3}$ and $E_b = L_w t$. L_w is the mechanical luminosity with which stellar winds and possible supernovae have introduced energy into the bubble. The estimated ages for the different source models, and the resulting energy input L_{SB} into the bubble are listed in the two right most columns in table 5.3.

5.2 Comparison with Stellar Input

Since, except for a single Wolf-Rayet *HD 32257* star at the west-edge (see fig. 3.6), there are no known O-type or other Wolf-Rayet stars within the bubble region, it is not possible to directly compare the contained energy to existing stellar inputs. In order to nevertheless put the calculated energy into perspective, the mechanical energy input through stellar winds L_w for the WR-star *HD 33257* and the LMC O-type star *BI 237* is calculated.

Table 5.4 lists the stellar type, effective temperature T_{eff}, mass-loss $\dot{M}$, and the stellar wind velocity v_∞ for the WR- and O-star, taken from Crowther et al., 2002, and Massa et al., 2017 respectively.

The mechanical luminosity L_w is given by

Table 5.4. Stellar and wind parameters for the stars *HD 32257* and *BI 237*. The parameters for *HD 32257* are taken from Crowther et al., 2002, and the parameters for *BI 237* are taken from Massa et al., 2017.

Star	Type	T_{eff} [kK]	$\dot{M}$ [$10^{-6}\ M_{\odot}\ yr^{-1}$]	v_{∞} [km s^{-1}]	L_{w} [10^{37} ergs s^{-1}]
BI 237	O2 V((f*))	51	3.88 ± 0.58	3400	1.42
HD 32257	WC4	71	12.6	2300	2.11

$$L_w = \frac{1}{2}\dot{M}\, v_{\infty}^2, \tag{5.2.1}$$

with the values given in the last column of table 5.4.

Comparing the mechanical luminosity L_w of the stars with the average luminosity in the bubble L_{SB}, one notices, that for the *nei* and two *apec* source models the L_{SB} values are an order of magnitude lower than the mechanical luminosity L_w of both stars. While it is unlikely that the stars maintain a constant energy output over the $\sim$ 1 Myr lifetime of the bubble, it is still a strong indicator, that the bubble is not caused by the combined stellar wind from a unknown group of massive stars.

At the same time, looking at figure 3.5 and 3.6, we see a clear outflow of hot diffuse X-Ray emitting gas to the east and west of the bubble region. This would obviously mean, that the energies given in table 5.3 underestimate the total energy that was introduced into the bubble.

5.3 Comparison with the [SII] to Hα Ratio

Figure 5.1 shows the ratio of [SII] to Hα emission, derived from the MCELS data, see Smith et al., 2005. The contour of the soft X-Ray emission is overlaid in white, while the bubble region is given in magenta.

The gas within the bubble region mainly holds a value $\sim$ 0.5, shown in green, with some small areas going above 0.7, visible in orange/red. This indicates, that the interior of the bubble can be considered to be, to some degree, shocked. The outflow regions to the east and north-west maintain large areas with a ratio values $\sim$ 0, suggesting no present shock. On the other hand, the northern part of the eastern outflow and the south-western outflow seem to be significantly shocked, with many spots showing ratio values > 0.7.

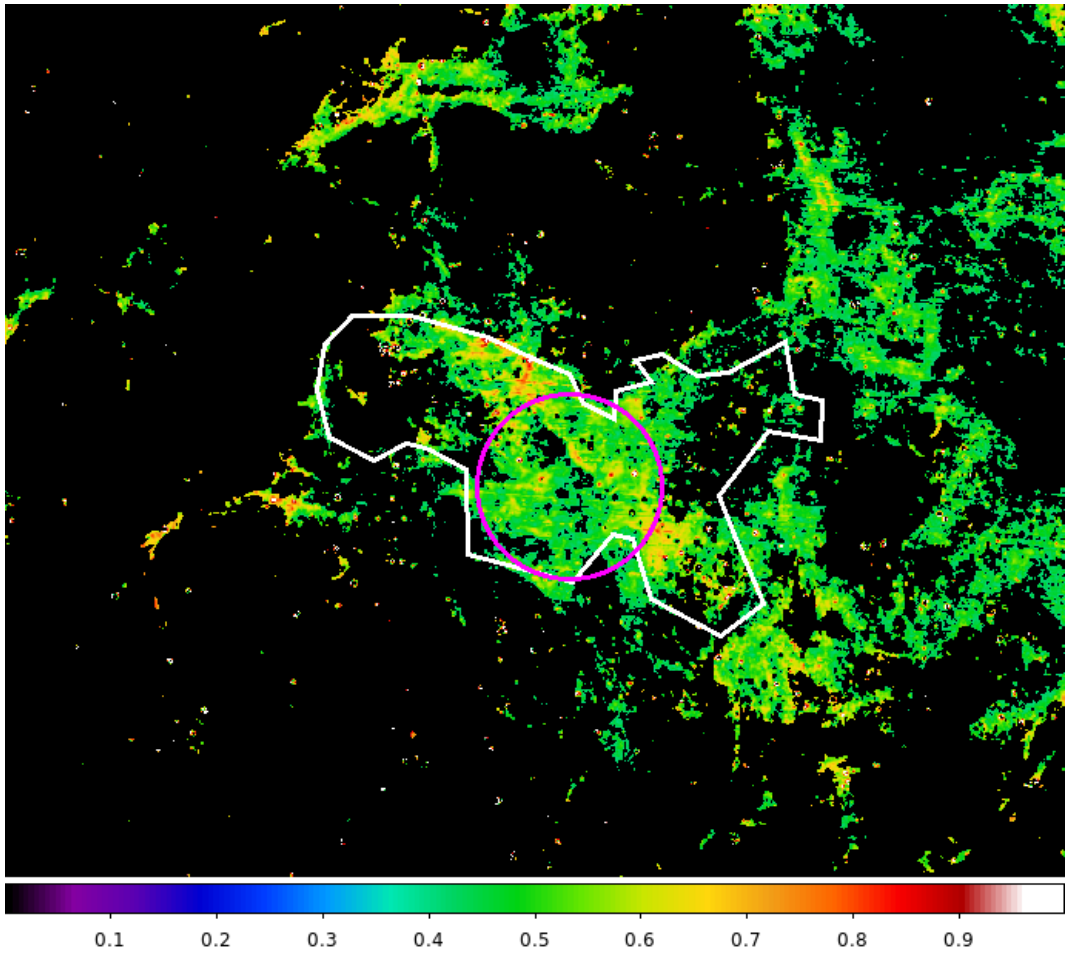

Figure 5.1: In this image the ratio of SII to Hα emission from the MCELS data (see Smith et al., 2005) is displayed. The contour of the soft X-Ray emission is overlaid in white, with the bubble region marked in magenta.

5.4 Comparison to Molecular Clouds

Grishunin et al., 2024, conducted a comprehensive mapping of molecular clouds in the LMC, by analyzing observations of the ^{12}CO(3−2) line conducted with the Large APEX sub-Millimetre Array (LAsMA).

Figure 5.2 shows a zoom-in of figure 1 from Grishunin et al., 2024, focused on the bubble region. The basis for the image is the MCELS data from Smith et al., 2005, onto which Grishunin et al., 2024, overlaid their CO moment-zero map, indicating molecular clouds, in green and blue. The blue regions mark contours of the CO map, that coincide with regions of bright Hα emission.

To the north of the bubble, one can find a dense grouping of clouds, with two clouds, that cor-

respond with bright Hα emission, within the bubble. Two additional molecular cloud regions find themselves to the south-west and -east of the bubble region. The molecular clouds around the bubble could have been shocked, which in turn may have triggered star formation.

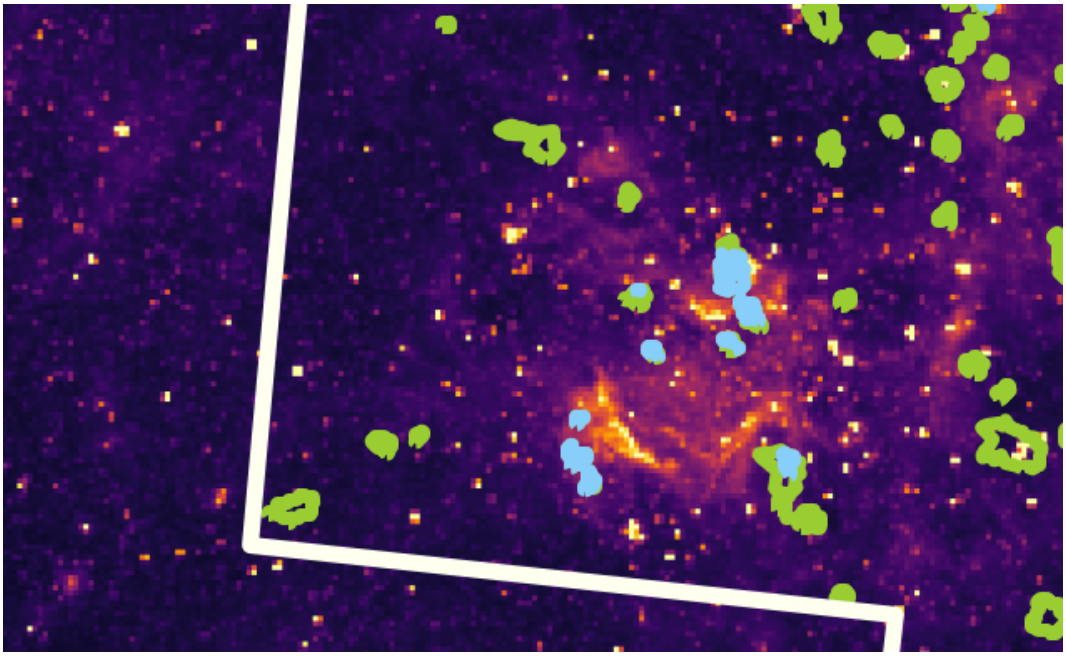

Figure 5.2: This image shows a zoom-in into figure 1 from Grishunin et al., 2024, focused on the bubble region. The basis for the image is the MCELS data from Smith et al., 2005, with green and blue marking the contours of the CO moment-zero map. The blue areas are regions of bright Hα emission that overlap with the CO contours. (Adapted from fig. 1 in Grishunin et al., 2024, ©the authors)

5.5 Conclusion

The X-Ray images (see fig. 3.5) clearly show a region of diffuse soft X-Ray emission that partially coincides with a shell-like structure in the optical images (see fig. 3.6). The X-Ray contour indicates an outflow to the east and west that seem to have broken through the shell, which is supported by the gaps, visible in the optical images.

The size of the shell like structure is $\sim$ 48 pc, which is comparable to the size of superbubbles, see Sasaki et al., 2011. At the same time it is possible, that we are presented with an old supernova remnant, which was the reason for the initial observation with XMM-Newton by Dr. Patrick Kavanagh. The absence of any known massive stars would point towards a SNR, possibly in combination with winds from the massive star, before the supernova.

Additional support for a supernova remnant can be found in the relatively low average energy input L_{SB} into the bubble, see table 5.3, that is exceeded by the mechanical energy input from solar winds of a single massive star, see table 5.4. A major caveat in the energy calculation, is the fact that the large outflow regions have most likely removed significant amounts of energy from the bubble region, making a direct energy comparison difficult.

Lastly, figure 5.1 shows, that the bubble region is, to a certain degree, shocked, with strong indicators for a shock to the north and south-west, where we also find groups of molecular clouds, see figure 5.2.

While, with the present data, no definite answer can be given to the question, if the shell-like structure belongs to a superbubble or supernova remnant, it may very well be a combination of the two. The shell could belong to a wind driven bubble, that was later broken through by a shock from a supernova, causing the outflows.

CHAPTER 6

Summary

The region south-west of the Large Magellanic Cloud, at the coordinates RA: $04^{h}57^{m}07.8^{s}$ and DEC: $-69°23'58.0''$, clearly shows a shell like structure in optical observations, see figure 3.6. Suspecting a possible supernova remnant, Dr. Patrick Kavanagh proposed and conducted an observation with the XMM-Newton X-Ray observatory (Obs-ID: 0841660301). In this work, the data obtained during that observation was used to create X-Ray images of the region, and to perform a spectral analysis of the X-Ray emission.

The data extraction was conducted using the XMMSAS software, following the *COOKBOOK FOR ANALYSIS PROCEDURES FOR XMM-NEWTON EPIC OBSERVATIONS OF EXTENDED OBJECTS AND THE DIFFUSE BACKGROUND*, provided by Snowden and Kuntz, 2024. Since the data is heavily flare contaminated, the automatic filtering was skipped, and a manual determination of the good-time-interval was performed. In order to filter the remaining flare contamination, a first fit was conducted with a single *apec* source component, see equation 4.1.1.

With the filtered data, three smoothed images were created, one in the soft band (300-1000 keV), one in the medium band (1000-2000 keV) and one in the hard band (2000-8000 keV), that were combined into a single RGB-image, see left image in figure 3.5. It was immediately obvious, that there is an extended region of diffuse soft X-Ray emission, that coincides with the shell-like structure, visible in the optical spectrum.

After confirming the presence of an X-Ray emitting region, the next step required the extraction of spectral data from said region. Since the shell-like structure was of special interest, an extraction region based on the optical data, together with the contour of the soft X-Ray emission, was defined, see figure 3.7. An additional extraction region was defined to the north, to allow for the background to be modeled and fitted simultaneously to the source.

The spectral analysis was performed for three different source models, a single *nei* compo-

nent, two *nei* and two *apec* components. The lowest Null-hypothesis probability was found for the two-*apec* model, with a value of 8.92×10^{-5}, indicating the presence of collisionally ionized plasmas of two distinct temperatures, see table 4.13.

In order to interpret the results of the spectral analysis, the energy content and average input were calculated for all source models, see table 5.3. These values were then compared to the mechanical luminosity, i.e. the mechanical energy input through solar winds, from a close-by Wolf-Rayet star and an LMC O-type star, see table 5.4.

The possible energy input from the stars was an order of magnitude greater than the required average input for the source region, making a purely wind driven bubble less likely. While the outflows may have removed a significant amount of energy from the source region, skewing the energy content within the shell to lower values, the lack of any known massive stars in the region would also point to an SNR rather than a bubble. At the same time one can not rule out, that a combination of a bubble, driven by winds from a massive star, and a later supernova from said star, could have caused the structure we observe now.

A comparison of the bubble region to a map of the [SII]-to-Hαratio, showed the gas inside the bubble to be moderately shocked, with a more pronounced shock-region in the north. At the same time, a recent mapping of molecular clouds in the LMC by Grishunin et al., 2024, revealed several areas with molecular clouds around the bubble, that could have been shocked.

In conclusion, it can not be said with absolute certainty, if the shell-like structure belongs to a supernova remnant or a wind driven bubble. The images and data indicate an older structure that most likely underwent one or more shocks in its history. The possibility, that the structure is a superbubble driven by both winds and supernovae would be supported by the current data.

Bibliography

Adelman, S. J., Robinson, R. D., & Wahlgren, G. M. (1993). Elemental Abundances of the B6 IV Star XI Octantis. *Publications of the Astronomical Society of the Pacific*, *105*, 327.

Anders, E., & Grevesse, N. (1989). Abundances of the elements: Meteoritic and solar. *Geochimica et Cosmochimica Acta*, *53*(1), 197–214.

Arnaud, K., Gordon, C., Dorman, B., & Rutkowski, K. (2023). *Xspec, An X-Ray Spectral Fitting Package*. HEASARC Astrophysics Science Division NASA/GSFC. Greenbelt, MD 20771.

Asplund, M., Grevesse, N., Sauval, A. J., & Scott, P. (2009). The Chemical Composition of the Sun. *Annual Review of Astronomy and Astrophysics*, *47*(1), 481–522.

Bonanos, A. Z., Massa, D. L., Sewilo, M., Lennon, D. J., Panagia, N., Smith, L. J., Meixner, M., Babler, B. L., Bracker, S., Meade, M. R., Gordon, K. D., Hora, J. L., Indebetouw, R., & Whitney, B. A. (2009). Spitzer SAGE Infrared Photometry of Massive Stars in the Large Magellanic Cloud. *The Astronomical Journal*, *138*(4), 1003–1021.

Bozzetto, L. M., Filipović, M. D., Vukotić, B., Pavlović, M. Z., Urošević, D., Kavanagh, P. J., Arbutina, B., Maggi, P., Sasaki, M., Haberl, F., Crawford, E. J., Roper, Q., Grieve, K., & Points, S. D. (2017). Statistical Analysis of Supernova Remnants in the Large Magellanic Cloud. *The Astrophysical Journal Supplement Series, Volume 230, Issue 1, article id. 2, 30 pp. (2017)*, *230*(1), Article 2, 2.

Chiappini, C., Romano, D., & Matteucci, F. (2003). Oxygen, carbon and nitrogen evolution in galaxies. *Monthly Notice of the Royal Astronomical Society*, *339*(1), 63–81.

Crowther, P. A., Dessart, L., Hillier, D. J., Abbott, J. B., & Fullerton, A. W. (2002). Stellar and wind properties of LMC WC4 stars. A metallicity dependence for Wolf-Rayet mass-loss rates. *Astronomy and Astrophysics*, *392*, 653–669.

Dahlem, M. (2023). *XMM-Newton Users Handbook - Issue 2.21*. European Space Agency - XMM-Newton Science Operations Centre.

Das, S., Mathur, S., Gupta, A., Nicastro, F., & Krongold, Y. (2019). Multiple Temperature Components of the Hot Circumgalactic Medium of the Milky Way. *The Astrophysical Journal*, *887*(2), Article 257, 257.

Edvardsson, B., Andersen, J., Gustafsson, B., Lambert, D. L., Nissen, P. E., & Tomkin, J. (1993). The Chemical Evolution of the Galactic Disk - Part One - Analysis and Results. *Astronomy and Astrophysics*, *275*, 101.

Gies, D. R., & Lambert, D. L. (1992). Carbon, Nitrogen, and Oxygen Abundances in Early B-Type Stars. *Astrophysical Journal*, *387*, 673.

Greenberg, J. M. (1974). The Interstellar Depletion Mystery, or where have all those Atoms Gone? *Astrophysical Journal*, *189*, L81.

Grishunin, K., Weiss, A., Colombo, D., Chevance, M., Chen, C. .-. R., Güsten, R., Rubio, M., Hunt, L. K., Wyrowski, F., Harrington, K., Menten, K. M., & Herrera-Camus, R. (2024). Observing the LMC with APEX: Signatures of large-scale feedback in the molecular clouds of 30 Doradus. *Astronomy and Astrophysics*, *682*, Article A137, A137.

HI4PI Collaboration, Ben Bekhti, N., Flöer, L., Keller, R., Kerp, J., Lenz, D., Winkel, B., Bailin, J., Calabretta, M. R., Dedes, L., Ford, H. A., Gibson, B. K., Haud, U., Janowiecki, S., Kalberla, P. M. W., Lockman, F. J., McClure-Griffiths, N. M., Murphy, T., Nakanishi, H., … Staveley-Smith, L. (2016). HI4PI: A full-sky H I survey based on EBHIS and GASS. *Astronomy and Astrophysics*, *594*, Article A116, A116.

Hickox, R. C., & Markevitch, M. (2006). Absolute Measurement of the Unresolved Cosmic X-Ray Background in the 0.5-8 keV Band with Chandra. *The Astrophysical Journal*, *645*(1), 95–114.

Hopkins, P. F., Quataert, E., & Murray, N. (2012). The structure of the interstellar medium of star-forming galaxies. *Monthly Notices of the Royal Astronomical Society*, *421*(4), 3488–3521.

Jansen, F., Lumb, D., Altieri, B., Clavel, J., Ehle, M., Erd, C., Gabriel, C., Guainazzi, M., Gondoin, P., Much, R., Munoz, R., Santos, M., Schartel, N., Texier, D., & Vacanti, G. (2001). XMM-Newton observatory. I. The spacecraft and operations. *Astronomy and Astrophysics, v.365, p.L1-L6 (2001)*, *365*, L1–L6.

Kilian, J. (1994). Chemical abundances in early B-type stars. V. Metal abundances and LTE/NLTE comparison. *Astronomy and Astrophysics*, *282*, 867–873.

Lodders, K. (2003). Solar System Abundances and Condensation Temperatures of the Elements. *The Astrophysical Journal*, *591*(2), 1220–1247.

Massa, D., Fullerton, A. W., & Prinja, R. K. (2017). Mass-loss rates from mid-infrared excesses in LMC and SMC O stars. *Monthly Notices of the Royal Astronomical Society*, *470*(3), 3765–3774.

Przybilla, N., Nieva, M.-F., & Butler, K. (2008). A Cosmic Abundance Standard: Chemical Homogeneity of the Solar Neighborhood and the ISM Dust-Phase Composition. *The Astrophysical Journal Letters*, *688*(2), L103.

Rathjen, T.-E., Naab, T., Girichidis, P., Walch, S., Wünsch, R., Dinnbier, F., Seifried, D., Klessen, R. S., & Glover, S. C. O. (2021). SILCC VI – Multiphase ISM structure, stellar clustering, and outflows with supernovae, stellar winds, ionizing radiation, and cosmic rays. *Monthly Notices of the Royal Astronomical Society*, *504*(1), 1039–1061.

Sasaki, M., Breitschwerdt, D., Baumgartner, V., & Haberl, F. (2011). XMM-Newton observations of the superbubble in N 158 in the LMC. *Astronomy and Astrophysics*, *528*, Article A136, A136.

Sasaki, M., Ponti, G., & Mackey, J. (2022). Diffuse Hot Plasma in the Interstellar Medium and Galactic Outflows. In *Handbook of x-ray and gamma-ray astrophysics* (p. 24).

Schartel, N., González-Riestra, R., Kretschmar, P., Kirsch, M., Rodríguez-Pascual, P., Rosen, S., Santos-Lleó, M., Smith, M., Stuhlinger, M., & Verdugo-Rodrigo, E. (2022). XMM-Newton. In *Handbook of x-ray and gamma-ray astrophysics* (p. 114).

Smith, R. C., Points, S. D., Chu, Y. .-., Winkler, P. F., Aguilera, C., Leiton, R., & MCELS Team. (2005). The Magellanic Emission Line Survey (MCELS). *American Astronomical Society Meeting Abstracts*, *207*, Article 25.07, 25.07.

Snow, T. P., & Witt, A. N. (1996). Interstellar Depletions Updated: Where All the Atoms Went. *Astrophysical Journal Letters*, *468*, L65.

Snowden & Kuntz. (2024). *COOKBOOK FOR ANALYSIS PROCEDURES FOR XMM-NEWTON EPIC OBSERVATIONS OF EXTENDED OBJECTS AND THE DIFFUSE BACKGROUND*. NASA/Goddard Space Flight Center. Greenbelt, MD 20771.

Sutherland, R. S., & Dopita, M. A. (1993). Cooling Functions for Low-Density Astrophysical Plasmas. *he Astrophysical Journal Supplement Series*, *88*, 253.

Tielens, A. G. G. M. (2005). *The Physics and Chemistry of the Interstellar Medium*.

Toalá, J. A., & Arthur, S. J. (2018). On the X-ray temperature of hot gas in diffuse nebulae. *Monthly Notices of the Royal Astronomical Society, Volume 478, Issue 1, p.1218-1230*, *478*(1), 1218–1230.

Tomkin, J., Woolf, V. M., Lambert, D. L., & Lemke, M. (1995). Carbon in Field F and G Disk Dwarfs. *Astronomical Journal*, *109*, 2204.

Weaver, R., McCray, R., Castor, J., Shapiro, P., & Moore, R. (1977). Interstellar bubbles. II. Structure and evolution. *Astrophysical Journal*, *218*, 377–395.

Wilms, J., Allen, A., & McCray, R. (2000). On the Absorption of X-Rays in the Interstellar Medium. *The Astrophysical Journal*, *542*(2), 914–924.

Yew, M., Filipović, M. D., Stupar, M., Points, S. D., Sasaki, M., Maggi, P., Haberl, F., Kavanagh, P. J., Parker, Q. A., Crawford, E. J., Vukotić, B., Urošević, D., Sano, H., Seitenzahl, I. R., Rowell, G., Leahy, D., Bozzetto, L. M., Maitra, C., Leverenz, H., … Pannuti, T. G. (2021). New optically identified supernova remnants in the Large Magellanic Cloud. *Monthly Notices of the Royal Astronomical Society, Volume 500, Issue 2, pp.2336-2358*, *500*(2), 2336–2358.

Zuo, W., Li, A., & Zhao, G. (2021). Interstellar Extinction and Elemental Abundances. *The Astrophysical Journal Supplement Series*, *252*(2), Article 22, 22.